Educing the source mechanism associated with downstream radiation in subsonic jets

F. Kerhervé, P. Jordan, A. V. G. Cavalieri, J. Delville, C. Bogey and D. Juvé

Journal of Fluid Mechanics / Volume 710 / November 2012, pp 606 - 640
DOI: 10.1017/jfm.2012.378, Published online: 31 August 2012

J. Fluid Mech. (2012), *vol.* 710, *pp.* 606–640.
doi:10.1017/jfm.2012.378

Educing the source mechanism associated with downstream radiation in subsonic jets

F. Kerhervé[1]†, P. Jordan[1], A. V. G. Cavalieri[1,2], J. Delville[1], C. Bogey[3] and D. Juvé[3]

[1] Institut PPRIME, CNRS UPR 3346, Université de Poitiers, ENSMA 86000, France

[2] Divisão de Engenharia Aeronáutica, Instituto Tecnológico de Aeronáutica, 12228-900 São José dos Campos, SP, Brazil

[3] Laboratoire Mécanique des Fluides et d'Acoustique, CNRS UMR 5509, Ecole Centrale de Lyon 69000, France

(Received 3 November 2011; revised 11 July 2012; accepted 21 July 2012; first published online 31 August 2012)

This work belongs to the ongoing debate surrounding the mechanism responsible for low-angle sound emission from subsonic jets. The flow, simulated by large eddy simulation (Bogey & Bailly, *Comput. Fluids*, vol. 35 (10), 2006a, pp. 1344–1358), is a Mach 0.9 jet with Reynolds number, based on the exit diameter, of 4×10^5. A methodology is implemented to educe, explore and model the flow motions associated with low-angle sound radiation. The eduction procedure, which is based on frequency–wavenumber filtering of the sound field and subsequent conditional analysis of the turbulent jet, provides access to space- and time-dependent (hydrodynamic) pressure and velocity fields. Analysis of these shows the low-angle sound emission to be underpinned by dynamics comprising space and time modulation of axially coherent wavepackets: temporally localized energization of wavepackets is observed to be correlated with the generation of high-amplitude acoustic bursts. Quantitative validation is provided by means of a simplified line-source *Ansatz* (Cavalieri *et al. J. Sound Vib.*, vol. 330, 2011*b*, pp. 4474–4492). The dynamic nature of the educed field is then assessed using linear stability theory (LST). The educed pressure and velocity fields are found to compare well with LST: the radial structures of these match the corresponding LST eigenfunctions; the axial evolutions of their fluctuation energy are consistent with the LST amplification rates; and the relative amplitudes of the pressure and velocity fluctuations, which are educed independently of one another, are consistent with LST.

Key words: aeroacoustics, jet noise

1. Introduction

The study of aeroacoustics, like that of complex fluid systems in general, is largely an exercise in system reduction. We wish to discern the essential features of the system with regard to an observable of interest (the radiated sound in the present case), the end objective being to come up with a simplified model of the flow. And, of course, it is a prerequisite that this simplified model provide as accurate as possible a prediction of the radiated sound field.

† Email address for correspondence: franck.kerherve@ec-lille.fr

This work presents an analysis methodology intended to achieve these goals. We consider that not all turbulence activity is of equal importance where sound generation is concerned, and that the problem of modelling comes down to the problem of identifying the flow (source) directions that can be removed without detrimentally affecting sound estimates. The analysis methodology involves the following steps.

(i) Obtain full or partial information associated with the complete flow solution, $\boldsymbol{q}$; this data could be provided by experimental measurements or from a numerical simulation (a numerical simulation is considered in this work).

(ii) Identify and extract, from $\boldsymbol{q}$, the observable of interest, $\boldsymbol{q}_A$; the low-angle sound radiation is considered here.

(iii) Construct an observable-based filter, $\mathscr{F}_{\boldsymbol{q}_A}$, which, applied to the full solution, removes information not associated with sound production, and thereby provides a reduced-complexity sound-producing flow skeleton, $\hat{\boldsymbol{q}}_D = \mathscr{F}_{\boldsymbol{q}_A}(\boldsymbol{q})$. Conditional analysis is used here, implemented by means of stochastic estimation.

(iv) Analyse $\hat{\boldsymbol{q}}_D$ with a view to postulating a simplified *Ansatz* for the source, $s(\hat{\boldsymbol{q}}_D)$.

(v) Ensure that the error function $\|\boldsymbol{q}_A - \hat{\boldsymbol{q}}_A\|_2$ is small, where $\hat{\boldsymbol{q}}_A = \mathscr{L}s(\hat{\boldsymbol{q}}_D)$, $\mathscr{L}$ being the convolution operator associated with solution of an inhomogeneous linear wave equation, and $s(\hat{\boldsymbol{q}}_D)$ the source term.

(vi) Determine the reduced-complexity dynamic law, $\hat{\mathscr{N}}(\hat{\boldsymbol{q}}_D) = 0$, that governs the evolution of $\hat{\boldsymbol{q}}_D$. (This aspect is partially treated in this paper, by means of linear stability theory, the real-time aspect of the problem being postponed to a second paper.)

Implicit in the above methodology is the assumption that turbulent flows can be meaningfully reduced to simplified kinematic and dynamic descriptions. A proposal of this kind put forth in 1952 would not have been very well received, as turbulence was then considered to comprise no more than a stochastic agglomeration of eddies. But much has changed since that time, both in terms of our understanding of turbulence, and the experimental and numerical diagnostics at our disposal for its analysis and modelling. In what follows we discuss briefly the notion of 'coherent structure': the interested reader can refer to Jordan & Colonius (2013) for a more complete review of coherent structures (wavepackets) in jet noise.

Experimental measurement and visualization of high Reynolds number jets reveals a chaotic multi-scale turbulence. Numerical simulations, such as the large eddy simulation (LES) used in this paper, continue to progress to finer and finer resolution, and in so doing they progressively capture more of these scales. Analysis of the turbulence so simulated leads to similar revelations regarding the wealth of space and time scales that populate the field. The visualization of vorticity, such as that shown in figure 2, is a nice example, and similar visualizations of more recent, higher-resolution simulations (Bailly, Bogey & Marsden 2010) show an even richer range of flow scales. There is no doubt, as measurements and visualizations as early as the 1950s had already suggested, that the turbulence of the jet comprises an extremely high-dimensional phenomenon. Computation of integral space and time scales, particularly in the azimuthal and axial directions, confirms that a significant portion of the fluctuation energy of the turbulence is dominated by motions that decorrelate rapidly both in space and in time.

Visualization and measurement from the 1960s through to today also leave no doubt that underlying this broadband field is a more organized motion. This motion cannot be clearly discerned in vorticity visualizations from simulations (vorticity tends to highlight smaller structures), nor is it readily accessible from spectral analysis of single- or multi-point hot-wire data. Certain kinds of visualization, measurement and data-processing do, however, reveal most clearly a more orderly component of the flow motion, with surprisingly high levels of axial, radial and azimuthal coherence. This order was first observed by Mollo-Christensen (1963) by means of pressure measurements in the irrotational near field; it is also readily observable from hot-wire and/or pressure measurements in the potential core region of the flow (Lau, Fisher & Fuchs 1972). Conditional analysis, which we use in this paper, is another effective way of educing the said structure from the confusion of the background turbulence (Moore 1977; Hussain & Zaman 1981).

State-of-the-art, high-resolution numerical simulations, if they are correct, should also contain this orderly component of the jet turbulence, and it should be discernible by means of precisely the same kinds of measurement, visualization and feature eduction techniques by which it has been so extensively studied, experimentally, for over 50 years.

There was much debate over the course of the 1970s, 1980s and 1990s as to what this orderly component of canonical free shear flows, such as jets and mixing layers, is exactly, and how important a role it plays in terms of the various mechanisms at work in the dynamics of turbulence: production, transport, dissipation, etc. Early conceptual scenarios comparing this component of the flow to the kinds of coherent vortical structures observed in transitional flows were dismissed by measurement, visualization and analysis (Dimotakis & Brown 1976; Chandrsuda *et al.* 1978; Yule 1978). The idea that the organized component might dominate turbulence dynamics was also dismissed; Hussain (1983) argues that the Reynolds stresses, vorticity and turbulence production associated with the coherent part of the turbulent jet is of the same order as that of the 'incoherent' part of the flow. We would contend that it is probably less important than this.

Probably the most satisfactory manner by which 'coherent structures' can be apprehended, and placed in an appropriate conceptual and theoretical framework, is to consider them, as did many early researchers, as linear instabilities that derive their energy from the mean flow. The physical argument implicit in this assumptions is that a scale separation exists between these large-scale, axially, radially and azimuthally coherent motions, and the smaller – but considerably more energetic – turbulent motions that scale with the local mixing-layer thickness. The estimate of Hussain & Zaman (1981), that these coherent motions span eight jet diameters in the axial direction – an estimate consistent with observations of Tinney & Jordan (2008) and Cavalieri *et al.* (2012*a*), for instance – supports the idea of a scale separation. There is of course no suggestion here that jet turbulence is somehow linear: the jet evolves as it does due to the nonlinear dynamics that underpin the rich range of scales present in the shear layer; and it is these nonlinear dynamics that establish the mean flow structure through the Reynolds stresses. This result of the nonlinear dynamics can be legitimately considered as a base flow about which a linearization can be performed, the scale separation argument being central, in which case the so-called 'coherent structures' can be understood as small-amplitude undulations of the jet about its mean state, these undulations being characterized by much larger space scales than the turbulence.

Where sound production is concerned, the salient feature of the orderly component of the flow motion is its large azimuthal and axial coherence, which means that despite its low fluctuation amplitude it can present an important flow motion where sound production is concerned: the acoustic efficiency of these motions is greater than that of the more energetic, but less coherent, smaller-scale motions, as first demonstrated, theoretically, by Michalke & Fuchs (1975).

A short overview of the different ways in which coherent structures (or wavepackets) have been studied is useful in order to clearly position the work we report here. Figure 1 illustrates three classes of study, indicated by the three boxes, that one encounters in the classical literature. The dotted line represents the broad spectrum of studies concerned, on one hand, with the challenge of identifying and educing wavepackets from turbulence and, on the other, with assessing the extent to which stability theory can constitute a suitable model. Mollo-Christensen (1963, 1967) observed wavepackets in his near-field pressure measurements, and suggested that hydrodynamic stability might be a useful means by which to model these; he also suggested how they might produce sound. Crow & Champagne (1971), Lau *et al.* (1972), Moore (1977) and Hussain & Zaman (1981) performed dedicated studies of the eduction of wavepackets from the turbulence of round jets. Crow & Champagne (1971), Crighton & Gaster (1976) and Moore (1977) made some of the first attempts to compare the educed wavepackets with linear stability theory; all of these studies involved comparisons with forced flows. Suzuki & Colonius (2006) and Gudmundsson & Colonius (2011) have reported more recent attempts to educe wavepackets, from unforced flows, and to confront them with the predictions of stability theory. We note, however, that none of the foregoing studies involve a serious attempt to quantitatively connect the wavepackets identified to the sound field: the studies all remain within the confines of the dotted square in figure 1.

Work has been reported where the connection is extended to the sound field (the dash-dotted box in figure 1). Tam & Morris (1980) and Tam & Burton (1984*a*,*b*) are examples, but all consider the supersonic scenario only; furthermore, quantitative comparisons were restricted to forced flows in Tam & Burton (1984*b*). The work of Mankbadi & Liu (1984) involves an attempt to extend from hydrodynamics to sound in a subsonic scenario, but turbulence data are not explicitly used, and no quantitative comparison is made with data.

A considerable body of work corresponding to that enclosed by the dashed line in figure 1 also exists. Papers studying the kinds of wavepacket behaviour that can lead to sound generation (wavepacket-to-sound arrow) include Crighton & Huerre (1990) and Sandham, Morfey & Hu (2006), but these papers do not include any comprehensive comparisons with data. Cavalieri *et al.* (2011*b*) explore how the details of time-local wavepacket dynamics can impact the sound field: this work involves quantitative comparison with LES data. Reba, Narayanan & Colonius (2010) have coupled near-field data, via a kinematic model of the wavepacket fluctuations registered on a Kirchhoff surface, to the far field. However, none of this work makes a theoretical connection to the turbulent jet.

A final body of work that must be cited also belongs within the confines of the dashed box in figure 1, but with the direction of the arrow reversed: work based on the use of far-field data to identify the parameters of a given wavepacket *Ansatz*. Papamoschou (2008), Morris (2009) and Papamoschou (2011) are good examples. Again, however, no rigorous theoretical connection is made to the turbulent jet.

The work we report here aims to bridge the gaps evoked above: we are working within the confines of the dash-dotted box, and the relevant arrow is that which connects the sound field to the dotted box. We use the sound field and the complete space–time structure of the turbulence to educe the sound-producing flow motions. We determine the parameters of a wavepacket *Ansatz* from this educed field; note that this

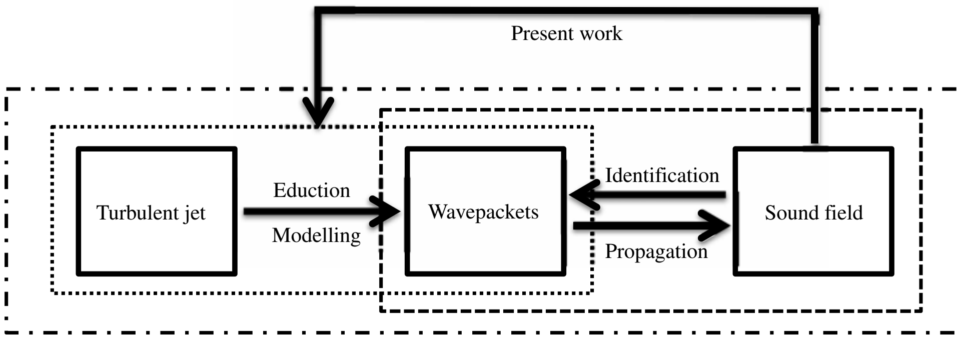

FIGURE 1. Schematic representation of research on coherent structures and jet noise.

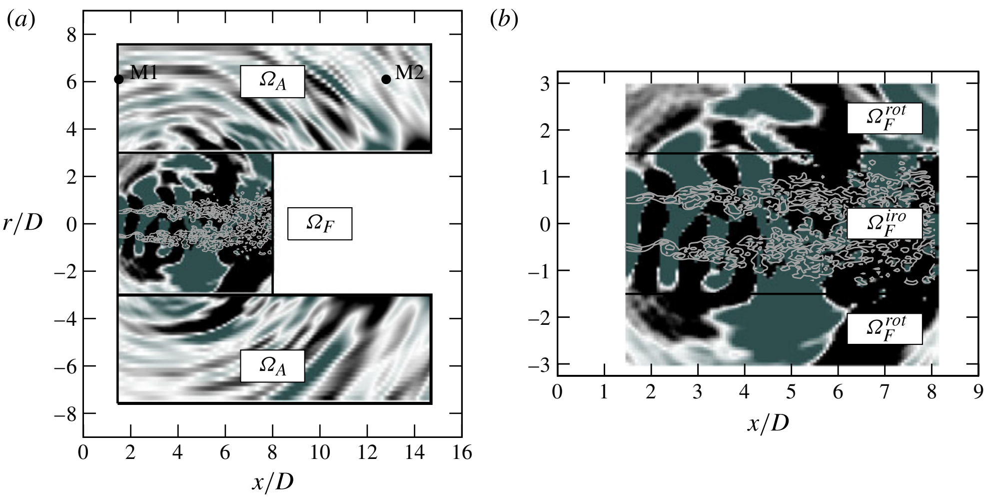

FIGURE 2. (Colour online) (*a*) Snapshot of vorticity field (grey line) and pressure field of the Mach 0.9 jet. Flow and acoustic regions Ω_F and Ω_A. (*b*) Breakdown of flow region Ω_F into Ω_F^{rot} and Ω_F^{iro} sub-regions.

is quite different from the determination of wavepacket parameters using approaches such as reported by Morris (2009) and Papamoschou (2011) where the problem is constrained only by the sound field; in our work the parameters are constrained both by the turbulence and the sound field. Finally, we make a theoretical connection to the flow by means of a confrontation of the educed field with the predictions of linear stability theory.

The paper is organized as follows. In § 2 the database is described. The low-angle sound emission, the observable of interest, $\boldsymbol{q}_A$, is isolated in § 3 using a frequency–wavenumber filter, and this enables the construction of the conditional filter, $\mathscr{F}_{\boldsymbol{q}_A}$, by means of linear stochastic estimation. This allows access to the flow skeleton, $\hat{\boldsymbol{q}}_D$, that underpins sound radiation. $\hat{\boldsymbol{q}}_D$ is analysed, in § 4 using proper orthogonal decomposition (POD) and in § 5 using wavelets. A simplified source *Ansatz*, $s(\hat{\boldsymbol{q}}_D)$, is proposed based on the results of the analysis. The source, a space- and time-modulated wavepacket, as proposed by Cavalieri *et al.* (2012*a*), is then tested, quantitatively,

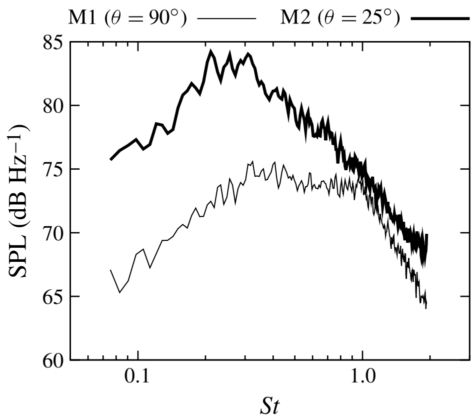

FIGURE 3. Sound pressure level in sideline and downstream directions at points M1 and M2 respectively as shown in figure 2(*a*).

by computing $\hat{\boldsymbol{q}}_A = \mathscr{L}s(\hat{\boldsymbol{q}}_D)$; good agreement is obtained when compared with the $\boldsymbol{q}_A$, showing how, for low-angle radiation, the jet can be considered as a line source driven by small-amplitude fluctuations of the axial velocity about its mean value. In § 6, the educed field is compared with the results of linear stability theory. The comparison includes the radial eigenfunctions and spatial amplification rates of both the velocity and pressure modes. Remarkable agreement shows that the educed field, already quantitatively validated with respect to sound production, can be considered as synonymous with linear instabilities of the mean flow. Section 7 closes the paper with some conclusions and perspectives.

2. Flow configuration

The flow investigated is a Mach 0.9 single-stream jet with Reynolds number – based on jet diameter and exit velocity – of 4×10^5, obtained from the large eddy simulation of Bogey & Bailly (2006*a*). Details of the simulation, as well as the flow and sound properties and their extensive validation, can be found in Bogey & Bailly (2006*a*,*b*,*c*,*d*, 2007).

For the present study, a two-dimensional x–r plane of the overall three-dimensional simulation is considered. Figure 2(*a*,*b*) shows instantaneous visualizations of the flow, vorticity and pressure being shown. A first split of the domain, into two parts, Ω_F and Ω_A, is performed; the challenge is to educe, from the full complexity of the fluid motions in Ω_F, those associated with the acoustic motions contained in Ω_A. Ω_F is then further split into Ω_F^{iro} and Ω_F^{rot}, as shown in figure 2(*b*), in which, respectively, irrotational and rotational motions dominate.

A total number of $N_t = 19\,000$ snapshots, sampled at a Strouhal number of $St_D = 3.9$ (corresponding to a total duration of $tU/D = 4900$), are considered. This long time-series is necessary to ensure convergence of the flow–acoustic and acoustic–acoustic correlations required for stochastic estimation. Block-averaging and overlapping-windowed Fourier transforms have been used to obtain these space–time correlations and their estimates at given time delay, as will be discussed further.

Sound spectra calculated for two observation angles relative to the jet axis, 90° and 25° (corresponding to points M1 and M2 in figure 2*a*) are shown in figure 3. On account of both the unresolved scales and the fact that the upstream boundary layer has not been simulated, the sideline spectrum is peakier than that observed experimentally. This work focuses on the downstream spectrum, whose peaky character is often argued to be due to the action of coherent structures.

3. Computing the sound-producing flow skeleton, $\hat{\boldsymbol{q}}_D$

The directive character of the sound field radiated by a round jet is frequently argued to be due to coherent structures (Mollo-Christensen 1963). However, it is not possible to provide a precise definition of what is meant by coherent structures, nor is there general agreement as to which aspects of their motion lead to the directive sound field produced by the round jet; see reviews of Jordan & Gervais (2008) and Jordan & Colonius (2013) and the introduction of Cavalieri *et al.* (2011*b*) for further discussion). The tool presented here is intended to provide clarification on this point. In this section steps (ii) and (iii) of the analysis methodology are described. First, the acoustic field is filtered so as to separate the low- and high-angle radiation; the low-angle component is considered to be the observable, $\boldsymbol{q}_A$. Stochastic estimation is then chosen as the observable-based filter, $\mathscr{F}_{\boldsymbol{q}_A}$, providing the conditional space–time flow fields (both pressure and velocity) associated with the low-angle sound emission.

3.1. *Directional filtering of the radiated sound field*

The radiated pressure field is filtered into two angular sectors ($0^\circ \leqslant \theta \leqslant 60^\circ$) and ($60^\circ \leqslant \theta \leqslant 120^\circ$), which are henceforth referred to, respectively, as $E_{30}(\boldsymbol{y}, t)$ and $E_{90}(\boldsymbol{y}, t)$. The filtering is effected in frequency–wavenumber space, (k_x, ω). For each radial position, y/D, the pressure field is Fourier-transformed from (x, t) to (k_x, ω):

$$\tilde{p}(y; \omega, k_x) = \iint_{-\infty}^{+\infty} p(x, y, t) \mathrm{e}^{-\mathrm{i}(\omega t - k_x x)} \, \mathrm{d}t \, \mathrm{d}x. \tag{3.1}$$

A bandpass filter associated with each of the angular sectors is then applied, which, for a given frequency, retains wavenumbers in the range $\omega/c(\theta_m) < k_x < \omega/c(\theta_M)$ where θ_m and θ_M are the limits of the angular sector considered, and $\mathrm{c}(\theta) = c_o/\cos(\theta)$ with c_o the speed of sound. For a given angular sector, the bandpass filter is defined as follows:

$$\mathscr{W}(\omega, k_x) = \begin{cases} \exp\left[-\left(k_x - \dfrac{|\omega|}{c(\theta_{M,i})} \right)^4 \Big/ \beta^4 \right] & \text{if } k_x \leqslant \omega/c(\theta_M), \\ 1 & \text{if } \omega/c(\theta_M) \leqslant k_x \leqslant \omega/c(\theta_m), \\ \exp\left[-\left(k_x - \dfrac{|\omega|}{c(\theta_{m,i})} \right)^4 \Big/ \beta^4 \right] & \text{if } \omega/c(\theta_m) \leqslant k_x, \end{cases} \tag{3.2}$$

where β is a coefficient used to control the abruptness of the bandpass window; its value here is $\beta = 5\mathrm{d}k_x$, where $\mathrm{d}k_x$ is the wavenumber resolution. The filtered pressure is recovered by inverse Fourier transform:

$$p_f(x, y, t) = \iint_{-\infty}^{+\infty} \tilde{p}(y; \omega, k_x) \mathscr{W}(\omega, k_x) \mathrm{e}^{\mathrm{i}(\omega t - k_x x)} \, \mathrm{d}\omega \, \mathrm{d}k_x. \tag{3.3}$$

Figure 4 shows frequency–wavenumber (left column) and space–time (right column) representations of the full pressure field (top), the E_{30} component (middle) and the E_{90} component (bottom). Both filtered fields exhibit a broad range of acoustic scales. The E_{30} component is considered as the observable, $\boldsymbol{q}_A$.

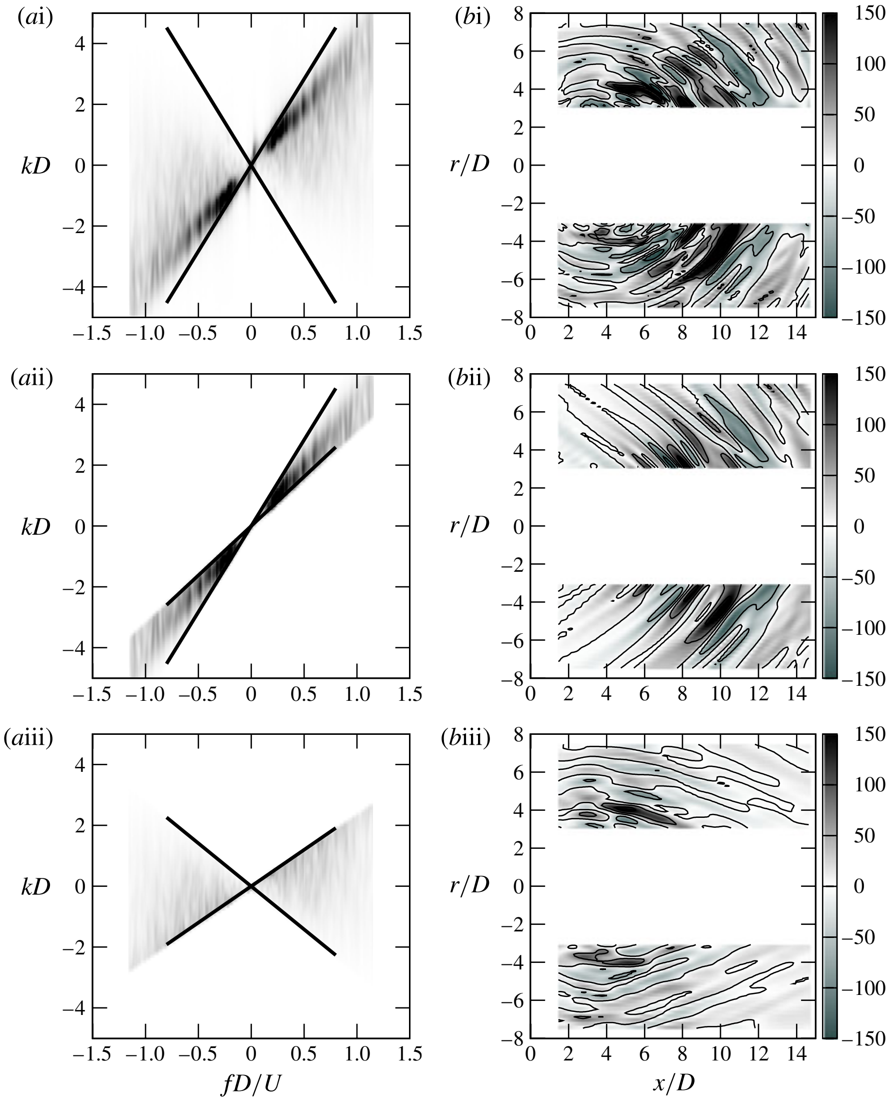

FIGURE 4. (Colour online) (*a*) Wavenumber–frequency power spectrum associated with: (i) overall radiated pressure field; (ii) $\boldsymbol{q}_A$, pressure field in angular segment 0–60°; and (iii) pressure field in angular sector 60–120°. (*b*) Associated snapshots of the three pressure fields.

3.2. *Linear stochastic estimation*

Stochastic estimation provides a means by which an approximation can be obtained for the conditional field $\langle \boldsymbol{q}(\boldsymbol{x}, t)|\boldsymbol{q}_A(\boldsymbol{x}', t')\rangle$ of some quantity $\boldsymbol{q}$ evaluated at point $\boldsymbol{x}$ and time t, given an observable $\boldsymbol{q}_A$ evaluated at $\boldsymbol{x}'$ and time t'.

In the problem considered, $\boldsymbol{q}(\boldsymbol{x}, t)$ comprises turbulent velocity and pressure fluctuations within the rotational part of the flow $\varOmega_F$, as well as the hydrodynamic pressure fluctuations in the irrotational near field. $\boldsymbol{q}_A(\boldsymbol{x}', t)$ is the filtered acoustic pressure field, E_{30}, in $\varOmega_A$. As shown in Adrian (1994), the linear estimate of the conditional average of $\boldsymbol{q}(\boldsymbol{x}, t)$, given $\boldsymbol{q}_A(\boldsymbol{x}'_i, t)$ in Ω_A, can be written as

$$\hat{\boldsymbol{q}}_D(\boldsymbol{x}, t) = \sum_{i=1}^{N} a(\boldsymbol{x}, \boldsymbol{x}'_i) q_A(\boldsymbol{x}'_i, t + \tau(\boldsymbol{x}, \boldsymbol{x}'_i)). \tag{3.4}$$

$\tau(\boldsymbol{x}, \boldsymbol{x}'_i)$ is the retarded time between points $\boldsymbol{x}$ in Ω_F and $\boldsymbol{x}'_i$ in Ω_A. The coefficients $a(\boldsymbol{x}, \boldsymbol{x}'_i)$ are obtained by solving, for a given point $\boldsymbol{x}$ in Ω_F, a linear system of equations of the form $\boldsymbol{Ay} = \boldsymbol{b}$ (Adrian 1994) with

$$\boldsymbol{y} = (a(\boldsymbol{x}, \boldsymbol{x}'_1), \ldots, a(\boldsymbol{x}, \boldsymbol{x}'_N))^{\mathrm{T}}, \tag{3.5}$$

$$\boldsymbol{b} = \left(\overline{q(\boldsymbol{x}, t) q_A(\boldsymbol{x}'_1, t + \tau(\boldsymbol{x}, \boldsymbol{x}'_1))}, \ldots, \overline{q(\boldsymbol{x}, t) q_A(\boldsymbol{x}'_N, t + \tau(\boldsymbol{x}, \boldsymbol{x}'_N))}\right)^{\mathrm{T}}, \tag{3.6}$$

$$A = \begin{bmatrix} \overline{q_A(\boldsymbol{x}'_1, t) q_A(\boldsymbol{x}'_1, t)} & \ldots & \overline{q_A(\boldsymbol{x}'_N, t) q_A(\boldsymbol{x}'_1, t + \tau(\boldsymbol{x}, \boldsymbol{x}'_1) - \tau(\boldsymbol{x}, \boldsymbol{x}'_N))} \\ \vdots & \ddots & \vdots \\ \overline{q_A(\boldsymbol{x}'_1, t) q_A(\boldsymbol{x}'_N, t + \tau(\boldsymbol{x}, \boldsymbol{x}'_N) - \tau(\boldsymbol{x}, \boldsymbol{x}'_1))} & \ldots & \overline{q_A(\boldsymbol{x}'_N, t) q_A(\boldsymbol{x}'_N, t)} \end{bmatrix} \tag{3.7}$$

and where the overbar denotes a time-average. The vector $\boldsymbol{b}$ contains flow–acoustic correlations while the matrix $\boldsymbol{A}$ contains acoustic–acoustic correlations.

The retarded time $\tau(\boldsymbol{x}, \boldsymbol{x}'_i)$ is the acoustic time delay between a point $\boldsymbol{x}$ in Ω_F and the point $\boldsymbol{x}_i$ in Ω_A. This is computed for each pair of points $(\boldsymbol{x}, \boldsymbol{x}'_i)$ by solving ray-tracing equations, following Bogey & Bailly (2007). A fourth-order Runge–Kutta scheme is used for temporal integration while mean-flow derivatives are calculated using centred fourth-order finite differences. Samples of calculated ray paths are shown in figure 5, giving a sense of the effect of mean-flow refraction.

Here $\boldsymbol{q}_A$ contains $N = 20 \times 14$ signals from the pressure probes distributed over Ω_F; these are indicated in figure 6 by black dots. With a view to obtaining an approximation of the axisymmetric component of the sound field, known to dominate downstream radiation (Michalke & Fuchs 1975; Fuchs & Michel 1978; Juvé, Sunyach & Comte-Bellot 1980; Cavalieri *et al.* 2011*b*), the pressure signals used in the stochastic estimation are obtained by averaging the upper and lower sections of Ω_A:

$$q_A(\boldsymbol{x}'_i, t) = q_A(x'_i, r'_i, t) = \tfrac{1}{2}[p_f(x'_i, |r'_i|, t) + p_f(x'_i, -|r'_i|, t)], \tag{3.8}$$

where (x'_i, r'_i) are the coordinates of $\boldsymbol{x}'_i$ and p_f the pressure fluctuations recorded at the probes.

Finally, the system of equations $\boldsymbol{Ay} = \boldsymbol{b}$ is solved for each point in Ω_F. In order to deal with an eventual ill-conditioning of the linear system, the solution $\tilde{\boldsymbol{y}}$ is obtained with the aid of a Tikhonov regularization as described in Cordier, Abou El Majd & Favier (2010).

3.3. *Domain breakdown*

Figure 6(*a*) shows the full LES solution at a given instant in time. The black dots in Ω_A indicate the locations of pressure probes used for the stochastic estimation. The pressure time histories of four pressure probes, located in Ω_A at $(x/D, y/D) = (3.5, \pm 6)$ and $(12.5, \pm 6)$ (black squares) are shown in the centre of the image. These are helpful for tracking acoustic signatures to and from the flow: an example of such analysis is presented later.

In Ω_A the pressure field, here entirely propagative, is shown. Ω_F^{iro} contains the near-field pressure, which comprises both propagative and non-propagative components. The latter, which carry the footprint of coherent structures (Tinney & Jordan 2008),

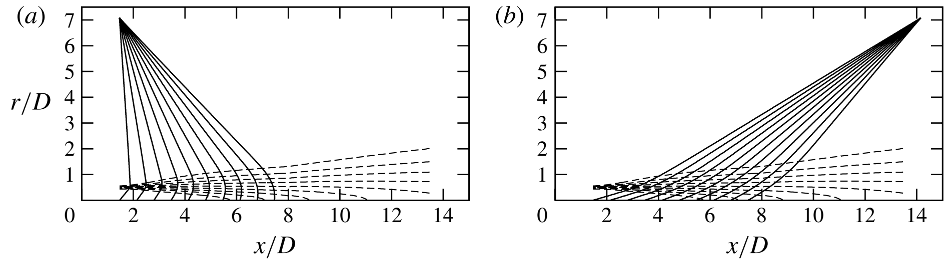

FIGURE 5. Solid lines, acoustic ray paths between a selection of points along the jet centreline and two different positions in the acoustic field; dashed lines, isocontours of mean axial velocity.

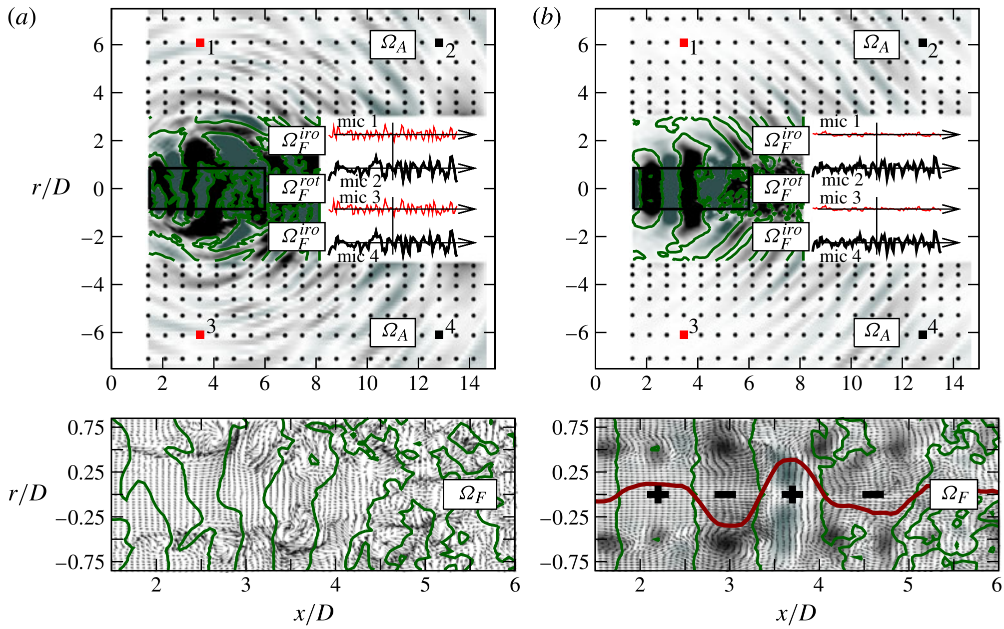

FIGURE 6. (Colour online) Pressure and velocity fields of (*a*) LES solution, $\boldsymbol{q}$, and (*b*) the observable, $\boldsymbol{q}_A$ (in Ω_A) and educed field, $\hat{\boldsymbol{q}}_D$ (in Ω_F^{irot} and Ω_F^{rot}). The upper figures show pressure only. The lower figures, which show the velocity field, are close-ups of the regions identified by black boxes in the upper figures. The shading here corresponds to the Γ criterion, the solid green lines are isocontours of zero pressure and the solid red line shows the centreline pressure signature (the y-direction in this case corresponds to the pressure amplitude.) The zones Ω_A, Ω_F^{iro} and Ω_F^{rot} correspond, respectively, to the linear acoustic region, the irrotational near field, where perturbations include acoustic and hydrodynamic components, and the nonlinear, vortical region. (*a*) LES solution at $tU/D = 120.7$; (*b*) linear stochastic estimation solution at $tU/D = 120.7$.

are frequently considered to be synonymous with linear instability waves (Suzuki & Colonius 2006) and have inspired a number of reduced-complexity source modelling methodologies (Sandham & Salgado 2008; Gudmundsson & Colonius 2009). Finally, in Ω_F^{rot}, both velocity and pressure fields are considered. The velocity field is best visualized in a Lagrangian reference frame, as per Picard & Delville (2000), by considering the quantity $\alpha u' + U - U_c$ with $\alpha = 10$ and $U_c = 0.55U_j$. The coefficient α is used to boost the fluctuation level so as to more clearly discern the flow topology. The green lines in Ω_F^{rot} are isocontours of zero pressure; by means of these, regions of positive and negative pressure can be seen within Ω_F^{rot}, i.e. the extension of the irrotational field of Ω_F^{iro} into the nonlinear, rotational region of the flow. Figure 6(*b*) will be discussed in what follows.

4. Results and discussion

A presentation of the flow skeleton, $\hat{\boldsymbol{q}}_D$, is provided in this section. In particular, proper orthogonal decomposition is used, to both discern the general structural features of the field and to provide an idea of the dimension of the associated phase-space.

4.1. *General presentation of* $\hat{\boldsymbol{q}}_D$

Figure 6(*b*) shows, in Ω_F^{iro} and Ω_F^{rot}, an instantaneous view of the conditional pressure and velocity fields of $\hat{\boldsymbol{q}}_D$. It should be noted that the pressure and velocity fields are computed independently. A first observation that can be made is that good continuity is maintained between zones Ω_F^{iro} and Ω_A (remember, zone Ω_F^{iro} in figure 6*b* is the reconstructed field, whereas zone Ω_A is the low-angle component of the LES solution), and this persists as the reconstruction and the filtered LES solutions evolve in time. This continuity is due to the fact that a purely linear relationship exists between pressure fluctuations in the region $|r/D| > 3$ and those in the region $2 < r/D < 3$; as the nonlinear region of the flow is approached, a progressive increase in differences is observed between the conditional fields and the LES solution. These are the differences we are interested in: the conditional fields constitute structural entities related to the sound field by means of a linear transfer function – a reduced-complexity subspace of the flow that is linearly mapped to the sound field.

Comparison of figures 6(*a*) and 6(*b*) gives a visual sense of the effect of applying stochastic estimation. While this will be evaluated quantitatively later, let us here note the eduction of an organized flow structure: large, axially organized, vortical structures, interspersed by saddle points. Furthermore, we see that the regions of negative and positive conditional pressure (computed independently of the velocity field) correspond, as one would expect, to the vortical cores and the saddle points. This qualitative physical consistency supports the idea that the flow skeleton educed, $\hat{\boldsymbol{q}}_D$, has properties of a Navier–Stokes solution, and could possibly be modelled as such. Further evidence of this will be presented in § 6.

The result shown in figure 6 is reminiscent of those obtained by the turbulence community in their attempts to separate 'coherent structures' from 'background turbulence' in various turbulent shear flows: turbulent boundary layers (Adrian 1977, 1978; Tung & Adrian 1980; Guezennec 1989; Zhou *et al.* 1999; Christensen & Adrian 2001; Stanislas, Perret & Foucault 2008), mixing layers (Delville *et al.* 1999; Ukeiley *et al.* 2001; Olsen & Dutton 2002; Druault, Yu & Sagaut 2010), cavity flows (Murray & Ukeiley 2005; Hudy & Naguib 2007; Murray & Ukeiley 2007), free jets (Jordan *et al.* 2005; Tinney, Glauser & Ukeiley 2005; Tinney *et al.* 2006, 2007). The present work differs from these studies in terms of the event data used. Rather than obtain conditional fields associated with turbulence quantities (summarized, for example, in Adrian 1994, table 1, p. 9), conditional fields associated with the radiated sound field are computed.

4.2. *Proper orthogonal decomposition of* $\hat{\boldsymbol{q}}_D$

A proper orthogonal decomposition of both the conditional flow field and the LES solution is performed in order to assess differences between the fields in terms of their respective space and time organizations. POD of $\hat{\boldsymbol{q}}_D$ is conceptually similar to the 'most observable decomposition' proposed by Jordan *et al.* (2007) and further developed by Schlegel *et al.* (2012); it also bears similarity to the implementation, by Freund & Colonius (2009), of POD using an acoustically weighted energy norm. In all cases the modal decomposition is conditioned with respect to the fluctuation energy of the acoustic field.

The Fredholm integral eigenvalue problem considered corresponds to the vector 'snapshot POD' of Sirovich (1987) for a regular mesh:

$$\int_T C(t, t')a^{(n)}(t')\,\mathrm{d}t' = \lambda^{(n)} a^{(n)}(t), \tag{4.1}$$

where $a^{(n)}(t)$ are the temporal coefficients, $\lambda^{(n)}$ are the eigenvalues and $C(t, t')$ represents the two-time correlation tensor, spatially averaged,

$$C(t, t') = \frac{1}{T}\iint_S \sum_{i=1}^{n_c} u_i(\boldsymbol{x}, t)u_i(\boldsymbol{x}, t')\,\mathrm{d}\boldsymbol{x}, \tag{4.2}$$

with n_c the number of components used to describe the velocity field and T the duration of the data set. Two axial and radial velocity components are considered. The eigenfunctions, $\Phi_i^{(n)}(\boldsymbol{x})$, are obtained by projection of the velocity field onto the coefficients, $a^{(n)}(t)$:

$$\Phi_i^{(n)}(\boldsymbol{x}) = \int_T a^{(n)}(t)u_i(\boldsymbol{x}, t)\,\mathrm{d}t \quad \text{with } i = 1, \ldots, n_c. \tag{4.3}$$

The algorithm is applied to data taken from Ω_F^{rot}. 512 snapshots are considered, corresponding to a duration $TU/D \simeq 132$. Two POD metrics are studied: the convergence of the POD eigenspectrum is used to assess the degree of organization of $\hat{\boldsymbol{q}}_D$ (this can be loosely related to the dimension of the number of degrees of freedom of the flow skeleton), while the POD eigenfunctions give an idea of the representative spatial scales and their topology.

4.2.1. *Eigenspectra*

Figure 7 shows the convergence of the POD eigenspectrum of $\boldsymbol{q}$ and $\hat{\boldsymbol{q}}_D$. The result is clear: the complexity of the LES data leads to an eigenspectrum with slow convergence (100 modes required to capture 70 % of the fluctuation energy), while the more organized structure manifest in $\hat{\boldsymbol{q}}_D$ is reflected in a more rapid convergence (10 modes to capture the same energy). This order of magnitude difference reflects the lower-dimensional nature of the sound-producing structure of the turbulent jet.

4.2.2. *Eigenfunctions*

The POD eigenfunctions are presented in figure 9 for both velocity components and in figure 8 for the pressure field. The pressure eigenfunctions exhibit, for both $\boldsymbol{q}_D$ and $\hat{\boldsymbol{q}}_D$, a wavepacket structure characterized by axial growth and decay, the peak occurring upstream of the end of the potential core. We note the more abrupt axial decay of the $\hat{\boldsymbol{q}}_D$ eigenfunctions; similar differences were observed by Freund & Colonius (2009) between their acoustically optimized and classical POD modes. The first two modes are consistent with an axisymmetric field, for both $\boldsymbol{q}_D$ and $\hat{\boldsymbol{q}}_D$. For the higher-order modes ($n \geqslant 2$), the LES solution exhibits behaviour consistent with a helical organization. Downstream radiation is predominantly axisymmetric and so this

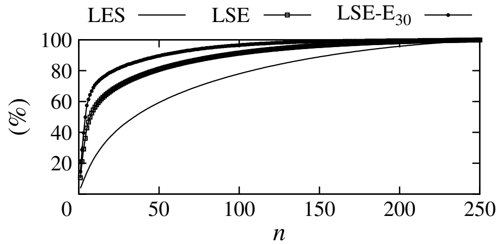

FIGURE 7. Convergence of POD eigenvalues for full and conditional velocity fields.

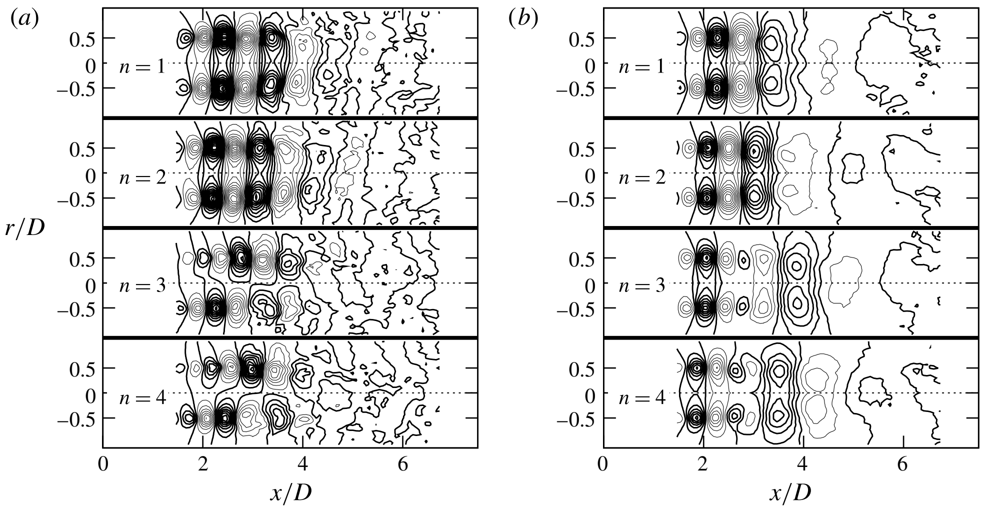

FIGURE 8. First four POD eigenfunctions of pressure fluctuations for (*a*) full LES and (*b*) $\hat{\boldsymbol{q}}_D$ solutions. Thin line, positive isocontours; thick line, negative isocontours: (*a*) LES Φ_p pressure; (*b*) $\hat{\boldsymbol{q}}_D$ Φ_p pressure.

difference is consistent: the helical organization present in the full LES solution is not efficient in driving downstream radiation, and is thus not educed by the conditional analysis.

The eigenfunctions associated with the velocity field exhibit considerable differences between $\boldsymbol{q}_D$ and $\hat{\boldsymbol{q}}_D$. The dominant $\hat{\boldsymbol{q}}_D$ eigenfunctions are structurally similar to the pressure eigenfunctions, again displaying features consistent with an axisymmetric wavepacket. The two most energetic $\boldsymbol{q}_D$ modes do not display such marked wavepackets, this organization appearing in the less energetic, higher-order modes. These characteristics are, again, similar to those observed by Schlegel *et al.* (2012) and Freund & Colonius (2009).

5. Source mechanism analysis

The conditional field, $\hat{\boldsymbol{q}}_D$, is now assessed with a view to gaining further insight regarding the flow motions associated with sound production. Following a methodology similar to that of Cavalieri *et al.* (2010, 2011*b*) and Koenig *et al.* (2011), a wavelet transform is used in order to identify temporally localized, high-amplitude

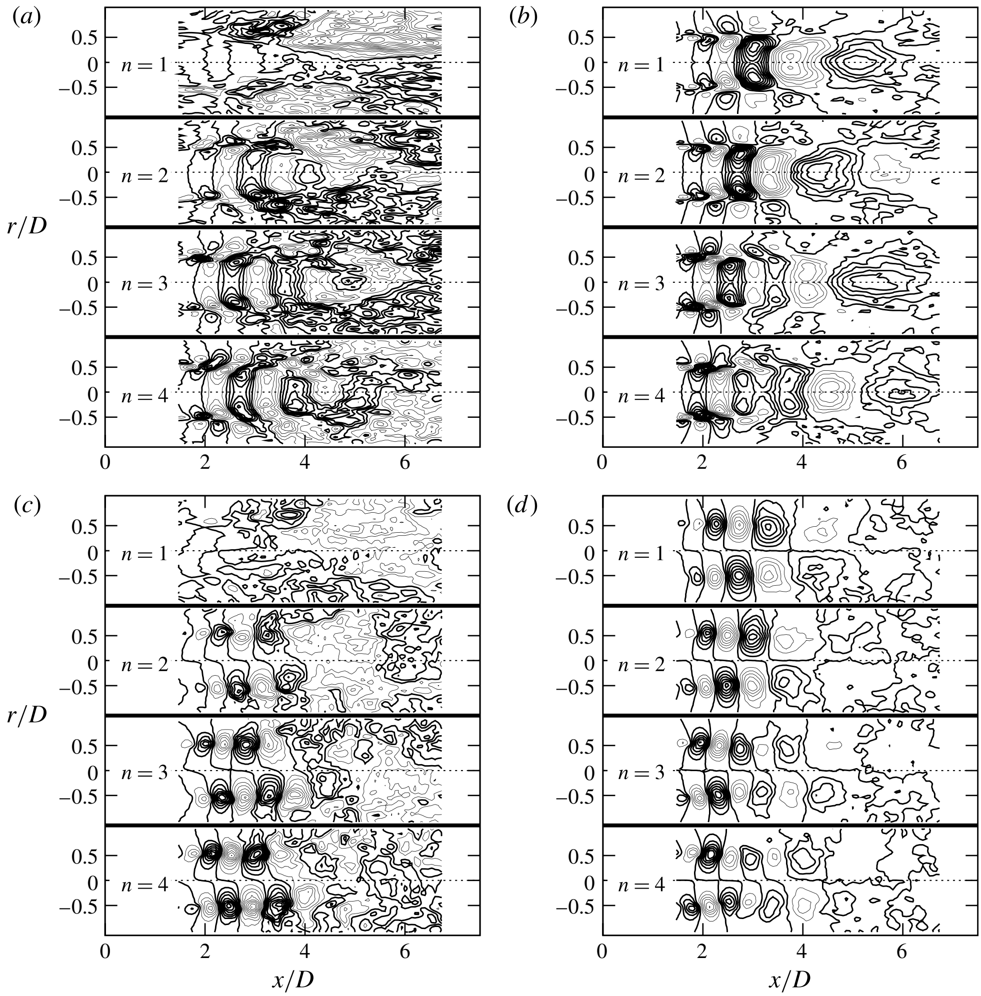

FIGURE 9. First four POD eigenfunctions for (*a*,*c*) full LES and (*b*,*d*) $\hat{\boldsymbol{q}}_D$ solutions. Thin line, positive isocontours; thick line, negative isocontours. (*a*,*b*) Longitudinal velocity; (*c*,*d*) transversal velocity components.

fluctuations in the low-angle sound emission; those fluctuations are then tracked back into the conditional flow field to discern the flow behaviour that led to their emission.

The continuous wavelet transform involves a projection of the pressure signal onto a set of basis functions that are localized in both time and time scale, being thus better adapted to the analysis of intermittent events than the Fourier basis. Further details regarding the wavelet transform can be found in Farge (1992).

The Paul wavelet is used, defined, at order m, as

$$\psi(1, t-\tau) = \frac{2^m \mathrm{i}^m m!}{\sqrt{\pi(2m)!}} \left[1 - \mathrm{i}(t-\tau)\right]^{-(m+1)}. \tag{5.1}$$

This was found by Koenig *et al.* (2011) to be well suited, with $m = 4$, to the analysis of jet noise.

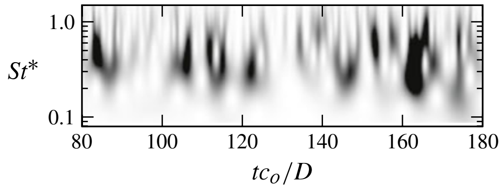

FIGURE 10. Scalogram of acoustic pressure for microphone M2 located at $\theta = 25°$.

The continuous wavelet transform of the pressure signal is

$$\tilde{p}(s, t) = \int_{-\infty}^{+\infty} p(\tau)\psi(s, t - \tau)\,\mathrm{d}\tau. \tag{5.2}$$

The scale s can be converted to a pseudo-frequency, as in Torrence & Compo (1998), or, equivalently, to a pseudo-Strouhal number, St^*, which for Paul's wavelet is

$$St^* = \frac{(2m+1)}{4s}\frac{D}{U}. \tag{5.3}$$

The scalogram, $|\tilde{p}(s, t)|^2$, is shown in figure 10 for a sensor located at $\theta = 25°$ and $6D$ (point M2 in figure 2) from the jet centreline. The most energetic bursts are found to occur at a pseudo-Strouhal number of ∼0.3, and a particularly loud event is observed, at this Strouhal number, at $tc_o/D = 164$. Let us examine the flow behaviour associated with this event.

Figure 11 shows the evolution of the flow up to and throughout the emission of the high-amplitude burst. The pressure field is shown in the upper part of each sub-figure, three pieces of information being contained in the lower part: the velocity vector field, shaded by the Γ criterion (dark shades correspond to rotational regions), isocontours of zero pressure (green lines), and the pressure on the jet centreline (red lines) – the y-direction here corresponds to the amplitude of this fluctuation. The evolution of the flow from $(t + t_{ray})c_o/D = 162.4$ to $(t + t_{ray})c_o/D = 165.3$ (where t_{ray} is the time taken for a sound wave to travel from the jet centreline, at $x/D = 4$, to the pressure sensor M2) comprises an axisymmetrization of the velocity field and an associated increase in both the amplitude and axial organization of the hydrodynamic pressure field. At $(t + t_{ray}c_o/D) = 162.4$ and $(t + t_{ray}c_o/D) = 163.8$ the coherent structures look disorganized, possibly in a helical arrangement. At $(t + t_{ray}c_o/D) = 165$ and $(t + t_{ray}c_o/D) = 165.3$ they become axially organized and axisymmetric, with a hydrodynamic pressure field comprising three high-amplitude spatial oscillations, consistent with the preferred structure of Hussain & Zaman (1981), the near-field signatures observed by Jordan & Tinney (2008) in co-axial jets, and the wavepackets identified experimentally and numerically, respectively by Cavalieri *et al.* (2011*a*, 2012*b*), as being associated with the low-angle axisymmetric component of jet noise. It appears to be this energization of the axisymmetric component of the flow that underpins the high-amplitude burst, the temporal growth and decay being particularly important, consistent with the simplified models of Sandham *et al.* (2006) and Cavalieri *et al.* (2011*b*).

Figure 12 allows an analysis over a longer period of time, where many such bursts are observed. Hydrodynamic and acoustic signatures are here temporally aligned using the propagation time, t_{ray}. The time evolutions of the centreline hydrodynamic pressure of $\boldsymbol{q}$ and $\hat{\boldsymbol{q}}_D$ are shown in the first two columns; the space–time modulation of organized wavepackets is most clearly visible in the latter. Columns (*e*) and (*f*) show, respectively, the time history of the acoustic pressure registered by the

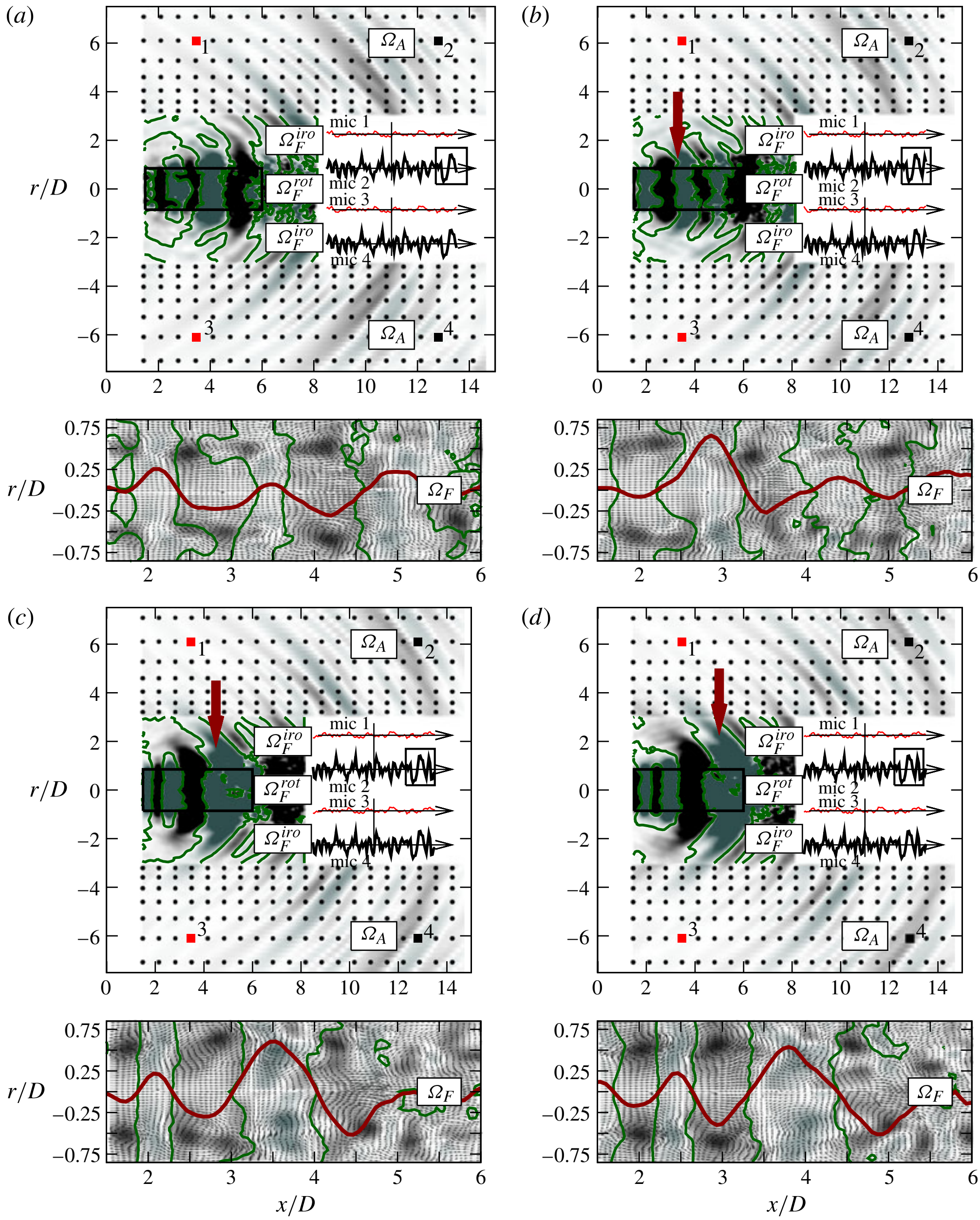

FIGURE 11. (Colour online) Conditional field, $\hat{\boldsymbol{q}}_D$, prior to and during the generation of a high-amplitude sound pressure fluctuation. The pressure time histories shown in the middle of the top part of each subfigure correspond to the pressure fluctuations registered on the probes indicated by the solid squares in the region Ω_A. A box in the top time trace (which corresponds to the low-angle probe) identifies the high-amplitude acoustic fluctuation. The arrow in subfigures (*b–d*) identifies this pulse as it is generated by, and begins to propagate from, the flow. The lower part of each subfigure shows a close-up of the rotational region Ω_F^{rot}, where velocity and pressure are shown (using the same display as in figure 6). The solid red line shows the amplitude of the fluctuating pressure on the jet centreline. (*a*) Step 1, $(t+t_{ray})c_o/D = 162.4$; (*b*) step 2, $(t+t_{ray})c_o/D = 163.8$; (*c*) step 3, $(t+t_{ray})c_o/D = 165.0$; (*d*) step 4, $(t+t_{ray})c_o/D = 165.3$.

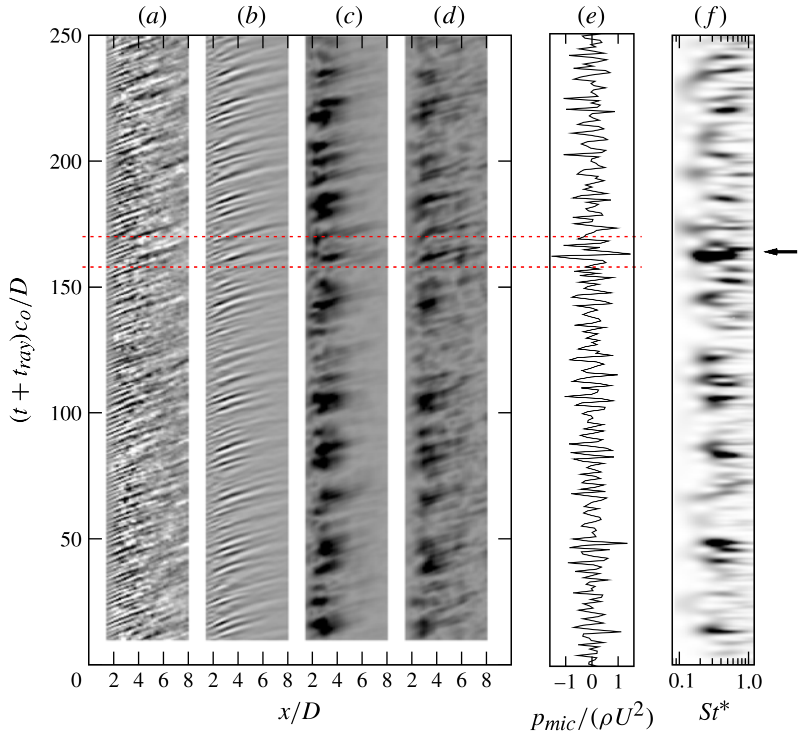

FIGURE 12. (Colour online) Space–time representation of instantaneous pressure fluctuations along the jet centreline: (*a*) calculated from LES; (*b*) obtained from conditional estimation using observable field E_{30}; (*c*) result of the short-time Fourier series of (5.4) applied to (*b*) and corresponding to the square root of the envelope $\phi_c^2(x, t) + \phi_s^2(x, t)$; (*d*) result of the short-time Fourier series applied to the radially integrated source term; (*e*) time history of the observer field E_{30} for sensor located in the far-field region at $x/D = 10$ and $y/D = 6$; (*f*) scalogram of (*e*). The black arrow on the right side identifies the highly noisy event discussed in § 5.

sensor M2 ($\theta = 25°$, $x = 6D$) and the corresponding scalogram (the same as that shown in figure 10, reproduced here to aid interpretation). Columns (*c*) and (*d*) will be commented on later.

The conditional hydrodynamic centreline pressure signature (column *b*) associated with the loud event discussed above can be seen to be temporally more abrupt (duration indicated by the dotted lines) than most of the other wavepacket modulations shown in column (*b*) (e.g. at $(t + t_{ray})c_o/D \approx 20, 50, 80, 145$). Our hypothesis is that these space and time modulations are associated with high acoustic efficiency. The corresponding wavepacket envelopes can be obtained by means of a short-time Fourier series as follows. For each axial position the temporal dependence of the pressure is assumed to contain a dominant harmonic oscillation ω with amplitudes slowly varying in time, as per Tadmor *et al.* (2008),

$$p(\boldsymbol{x}, t) = \phi_c(\boldsymbol{x}, t)\cos(\omega t) + \phi_s(\boldsymbol{x}, t)\sin(\omega t), \tag{5.4}$$

where the functions ϕ_c and ϕ_s are given by

$$\phi_c(\boldsymbol{x}, t) = \frac{2}{T}\int_{-T/2}^{+T/2} p(\boldsymbol{x}, t + \tau)\cos(\omega\tau)\,\mathrm{d}\tau, \tag{5.5a}$$

$$\phi_s(\boldsymbol{x}, t) = \frac{2}{T}\int_{-T/2}^{+T/2} p(\boldsymbol{x}, t+\tau)\sin(\omega\tau)\,\mathrm{d}\tau. \tag{5.5b}$$

The result, shown in column (*c*), provides the space and time dependence of the wavepacket envelope using the hydrodynamic pressure as the metric. In order to assess if these modulations are the salient features *vis-à-vis* sound production, it is necessary to compute a sound source quantity and evaluate, quantitatively, the relationship between the wavepacket envelope modulation and the radiated sound. This is done using the line source model of Cavalieri *et al.* (2011*b*).

The *Ansatz* takes the form

$$T_{11}(x, t) = 2\pi\left(\int \rho_0 U(x, r)\tilde{u}(x, r, t) r\,\mathrm{d}r\right)\delta(r), \tag{5.6}$$

with the integral term expressed as a wavepacket of the form

$$Q(x, t) = A(t)\exp[\mathrm{i}(\omega t - kx)]\exp\left[-\frac{x^2}{L(t)^2}\right], \tag{5.7}$$

which produces the far-field sound signature

$$p(\boldsymbol{y}, t) = -\frac{(kM_c)^2 A^* L^* \sqrt{\pi}\cos^2\theta}{|\boldsymbol{x}|} \times \exp\left[-\frac{(L^* k)^2 (1 - M_c\cos\theta)^2}{4}\right]\exp\left[-\mathrm{i}\omega\left(t - \frac{|\boldsymbol{x}|}{c_o}\right)\right], \tag{5.8}$$

where * denotes evaluation at the retarded time $t - |\boldsymbol{x}|/c_o$. The source is a non-compact axial distribution of axially aligned longitudinal quadrupoles that form a subsonically convected wavepacket. Only the linear component is modelled, as this has been shown in a number of studies to dominate low-angle radiation (Freund 2003; Bodony & Lele 2008; Sinayoko, Agarwal & Hu 2011). The radial integral, which allows the source to be concentrated on a line, is justified because of the radial acoustic compactness of the flow for the frequencies considered ($St \sim 0.3$). For further discussion and details the reader can refer to Cavalieri *et al.* (2011*b*).

The space–time wavepacket modulation discussed above appears in the model in the form of a time-varying amplitude, $A(t)$, and length scale, $L(t)$. These allow the convected wavepacket to be modulated in a manner similar to that observed in the conditional fields above. In what follows, the velocity components of the conditional field, $\hat{\boldsymbol{q}}_D$, are used to provide time-varying amplitudes and length scales for the source model. In order to do so a number of steps are necessary. Following computation of the radial integral in (5.6), proper orthogonal decomposition is applied, in the same spirit as § 4, and a twenty-mode truncation, comprising 99 % of the fluctuation energy, is retained. The result of this decomposition is then bandpass-filtered in the range $0.15 \leqslant St \leqslant 0.55$, which corresponds to the loud events identified in the scalogram. The dominant frequency and convection velocity (which provide ω and k) are obtained from this bandpass-filtered, twenty-mode truncation. A short-time Fourier series is then applied – similar to that applied to the centreline pressure and shown in figure 14(*c*) – in order to obtain space- and time-dependent wavepacket envelope amplitudes; the result is shown in figure 14(*d*) (we note the structural similarity to figure 14). At each time step, the result of the short-time Fourier transform is fitted with a Gaussian function (figure 13). This allows the space- and time-dependent wavepacket envelope to be expressed in terms of a time-dependent amplitude, $A(t)$, and length scale, $L(t)$.

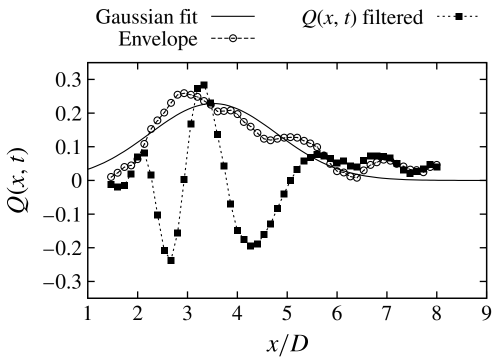

FIGURE 13. Envelope at a given time step of the integrated source volume of (5.7).

(a) $\boldsymbol{q}(x, t) \rightarrow$

(b) $\hat{\boldsymbol{q}}_D(x, t) \rightarrow$

(c) *Ansatz* $\rightarrow$

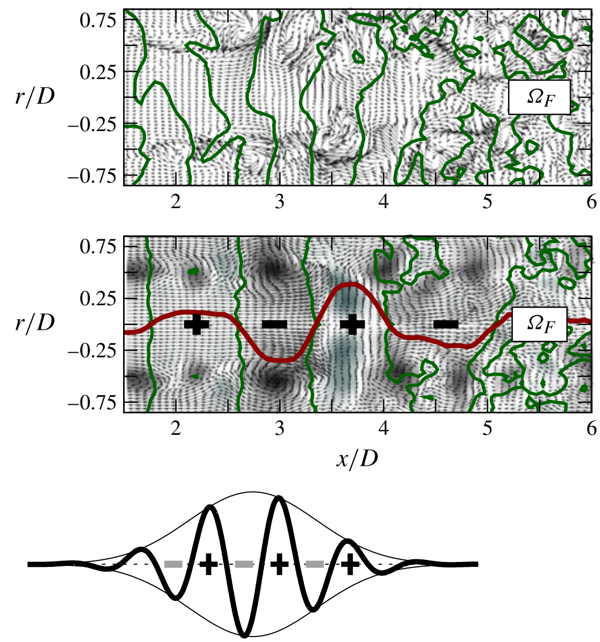

(d) $T_{11}(x, t) = 2\rho_0 Q(x, t)\delta(r)$ with $Q(x, t) = A(t)\exp[\mathrm{i}(\omega t - kx)]\exp\left[-\dfrac{x^2}{L(t)^2}\right]$

(e) $p(\boldsymbol{y}, t) = -\dfrac{(kM_c)^2 A^* L^* \sqrt{\pi}\cos^2\theta}{|\boldsymbol{x}|}\exp\left[-\dfrac{(L^* k)^2(1 - M_c\cos\theta)^2}{4}\right]\exp\left[-rmi\omega\left(t - \dfrac{|\boldsymbol{x}|}{c_o}\right)\right]$

FIGURE 14. (Colour online) Résumé of system reduction and analysis: (*a*) full flow solution, $\boldsymbol{q}$, showing velocity vectors and isocontours of zero pressure; (*b*) simplified flow skeleton $\hat{\boldsymbol{q}}_D$, obtained by conditional averaging (linear stochastic estimation); (*c*) schematic of line source *Ansatz*, $s(\hat{\boldsymbol{q}}_D)$, constructed from $\hat{\boldsymbol{q}}_D$; (*d*) mathematical expression for line source; (*e*) solution for radiated sound obtained using simplified source.

The sound field is then computed from (5.8) and compared with the LES, which is bandpass-filtered in the same way as the source.

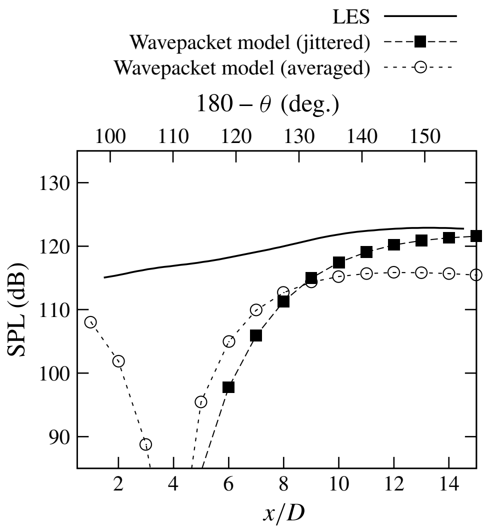

FIGURE 15. Comparison of acoustic signatures of 'jittering' (with amplitude modulation as per figures 12*b* and 13) and non-jittering wavepackets with that of the original LES.

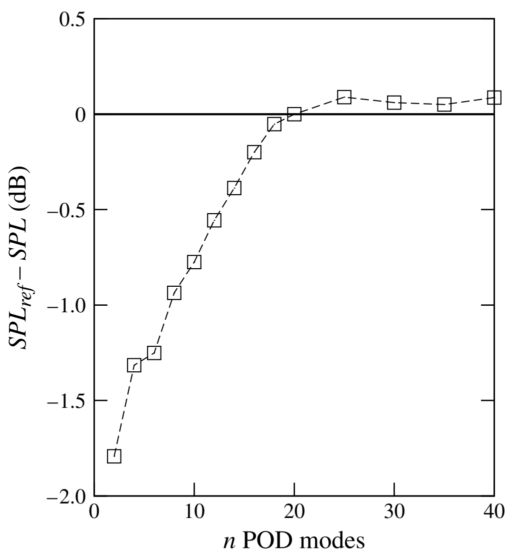

FIGURE 16. Difference in noise level estimate as a function of number of modes retained in POD reconstruction of the line source term. Observation angle $\theta = 25^{\circ}$. The reference level is taken from the modelled directivity obtained with 20 POD modes (figure 15).

Before going on to look at the result, let us here briefly summarize, schematically (figure 14), the entire data-reduction and analysis procedure. Following figure 14 from top to bottom: beginning with full flow information from the LES solution, $\boldsymbol{q}$, the sound-producing flow skeleton, $\hat{\boldsymbol{q}}_D$ (defined here as a conditional field with respect to the low-angle sound emission), is educed; based on an argument of radial acoustic compactness this field is concentrated on a line by means of a radial integral. The

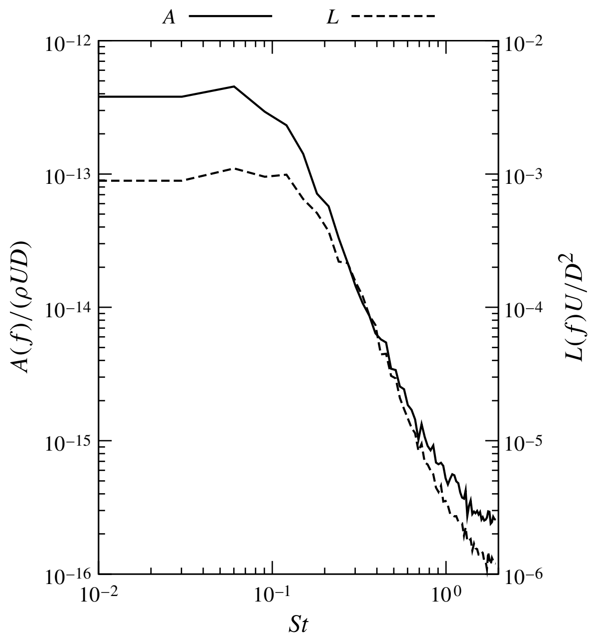

FIGURE 17. Spectra of coefficients $A(t)$ and $L(t)$ of the fitted wavepacket of (5.7).

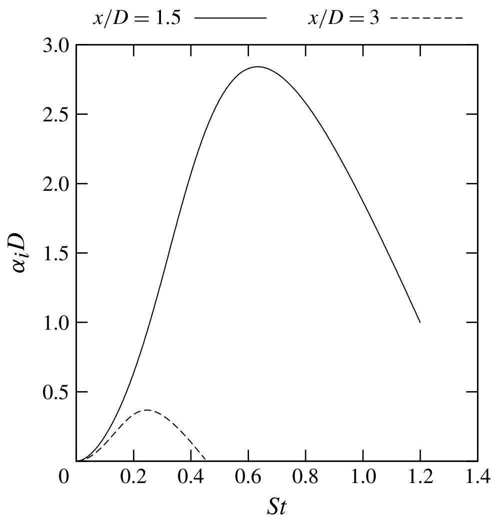

FIGURE 18. Growth rate of LST as a function of Strouhal number for $x/D = 1.5$ and $x/D = 3$.

result is truncated (20 POD modes retained), bandpass-filtered, and fitted to the source *Ansatz*. An analytical solution is available for the sound field radiated by the model source, and this is compared with the sound field of the LES (in the same frequency range).

The comparison is shown in figure 15. Three curves are shown: the solid black line corresponds to the bandpass-filtered sound field of the LES, the open circles show the

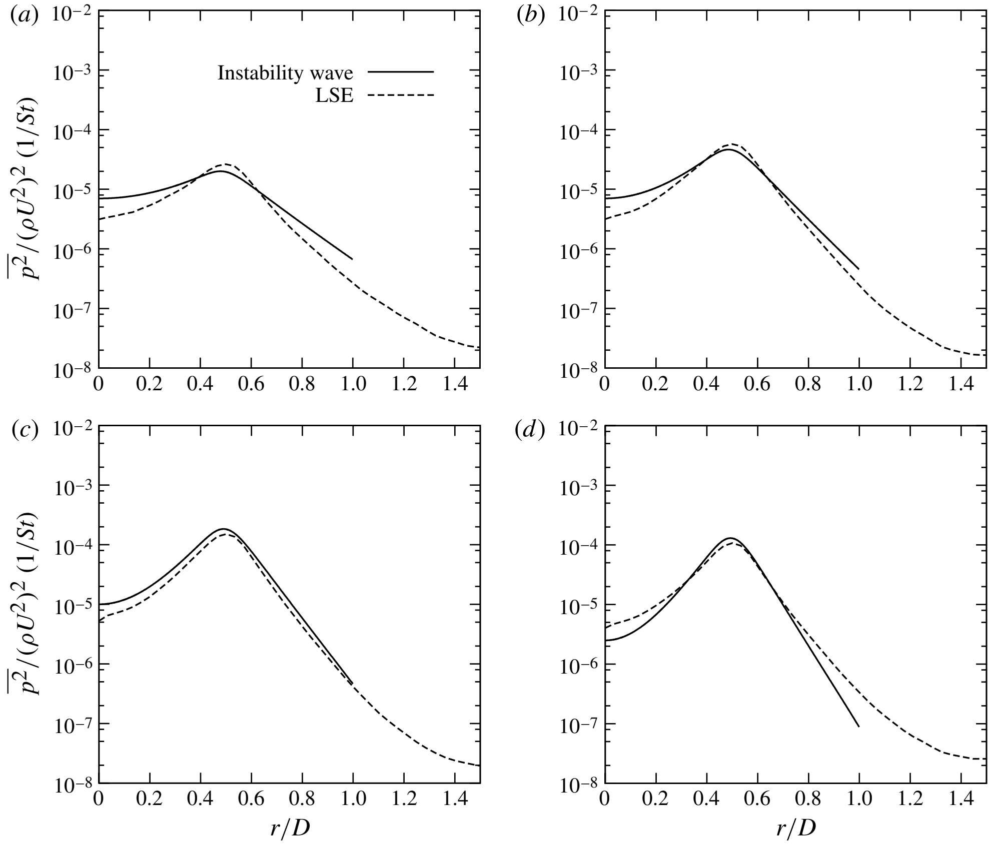

FIGURE 19. Comparison between pressure eigenfunctions of linear stability theory and the pressure field computed by LSE at $x/D = 1.5$ for Strouhal numbers of (*a*) 0.40, (*b*) 0.50, (*c*) 0.60 and (*d*) 0.70.

result obtained when time-averaged values of $A(t)$ and $L(t)$ are used, and the solid black squares show the result obtained from the procedure outlined above. The result is clear, and similar to that obtained by Cavalieri *et al.* (2011*a*): when the space–time modulation of the wavepacket envelope is suppressed, an error of over 6 dB results. On the other hand, when the wavepacket envelope is permitted to dance in a manner similar to the educed flow skeleton, agreement between the model sound field and the LES is good, showing that the behaviour educed by the conditional analysis constitutes salient sound source activity.

The fitting of the source model involves a certain degree of *ad hoc* choice, and so we perform some checks with a view to assessing the model's robustness. The least objective aspect of the fitting procedure is the POD truncation, and so we evaluate the sensitivity of the result to this. Figure 16 shows the differences in computed sound pressure level (SPL), at $\theta = 25^{\circ}$, between the twenty-mode model presented above and models with different numbers of modes. A maximum error of 1.8 dB is observed when only two modes are retained, a clear convergence being observed for $n > 20$. This result shows that the model is relatively robust and, furthermore, justifies the twenty-mode truncation.

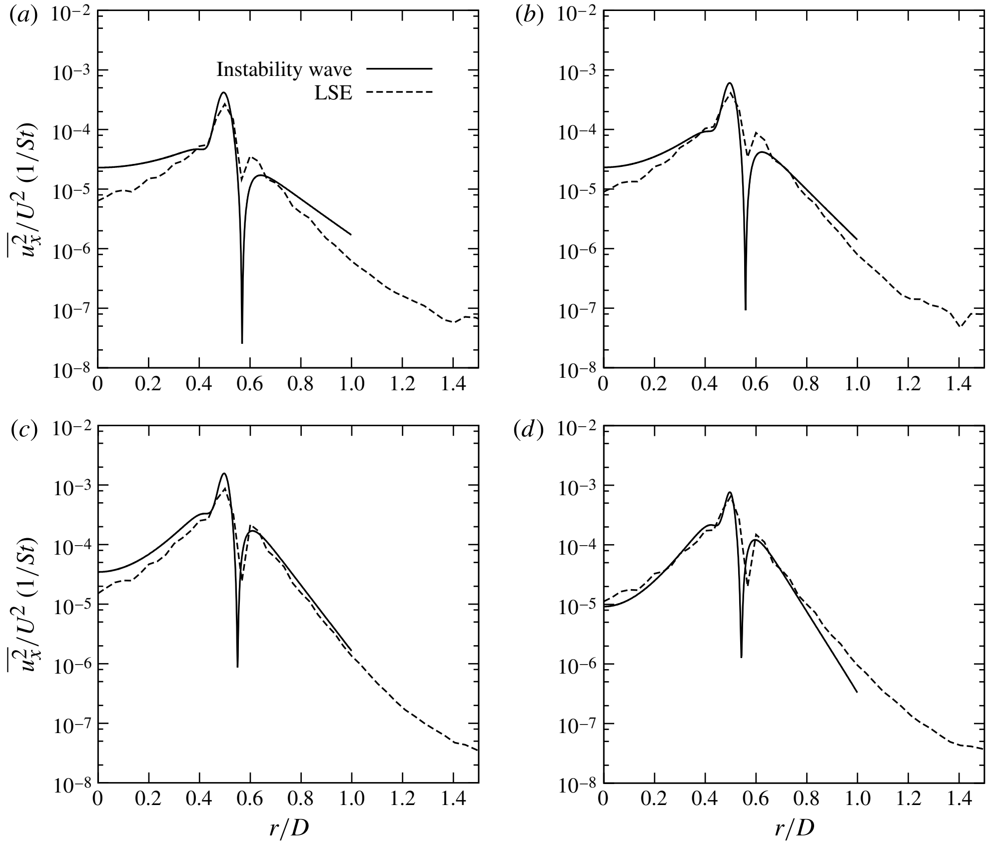

FIGURE 20. Comparison between u_x eigenfunctions of linear stability theory and the u_x component of the velocity field computed by LSE at $x/D = 1.5$ for Strouhal numbers of (*a*) 0.40, (*b*) 0.50, (*c*) 0.60 and (*d*) 0.70.

We perform the following further test, intended to evaluate the effect of contaminating the educed physics, and thereby testing the model further with regard to its physical pertinence. The key source parameters are the temporal modulation of both the amplitude and the axial extent of the wavepacket. Figure 17 shows the corresponding spectra, which are dominated by low-frequency activity; a further key characteristic (not shown) is a high level of correlation between $A(t)$ and $L(t)$ (coherence levels of the order of 80 % are observed in the energy-containing frequency band). We compute the sound field generated by a wavepacket whose envelope has the same power spectra, $A(f)$ and $L(f)$, as the educed model, but where the coherence between the two parameters is equal to zero (this is achieved through the imposition of a random phase on $A(f)$ and $L(f)$). The new wavepacket generates downstream radiation which is 2.3 dB less than that of the wavepacket with 'correlated modulation'. This result, considered together with the results of Cavalieri *et al.* (2011*a*,*b*), where the same source model produced close quantitative agreement when used in conjunction with data from two other numerical simulations (direct numerical simulation and LES), reinforce the contention that this correlated wavepacket modulation constitutes acoustically important source behaviour.

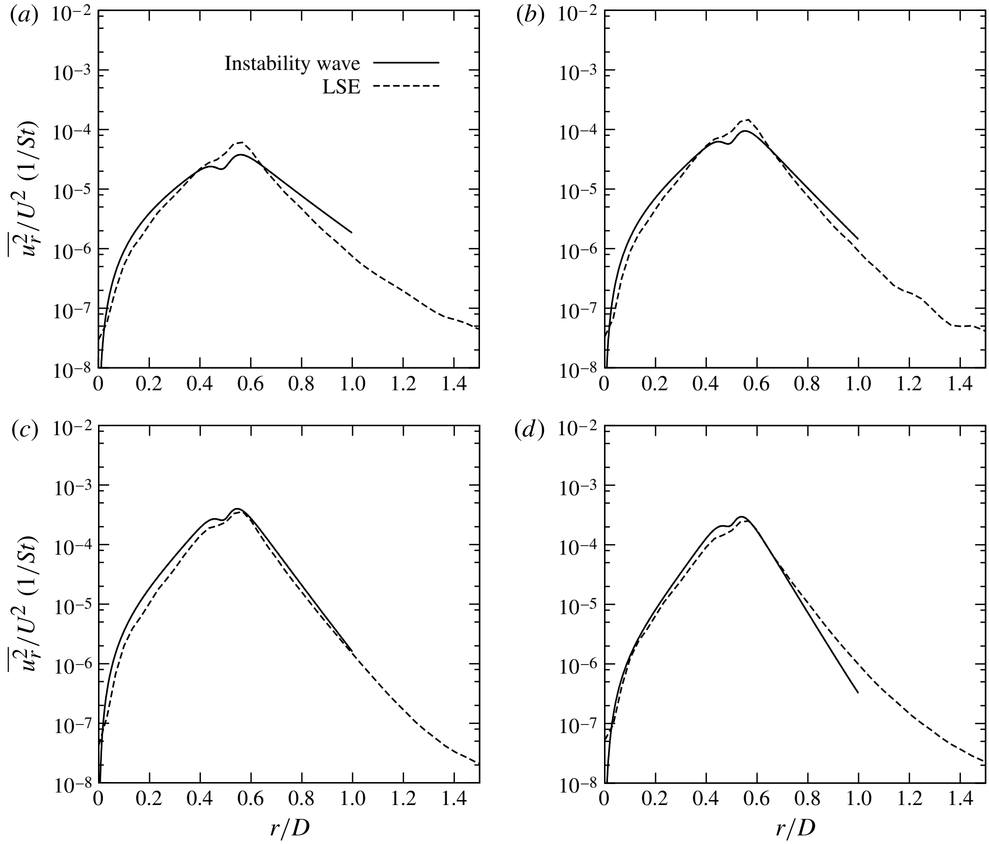

FIGURE 21. Comparison between u_r eigenfunctions for linear stability theory and LSE at $x/D = 1.5$ for Strouhal numbers of (*a*) 0.30, (*b*) 0.35, (*c*) 0.40, (*d*) 0.50.

6. Comparison of the estimated fields with linear instability waves

In keeping with the analysis approach outlined in § 1, we now perform some interrogations regarding the dynamic nature of the conditional fields obtained and validated as a sound source in the previous section. It was remarked earlier that, despite the fact that the conditional velocity and pressure fields are computed independently, the visualizations suggest that they behave in a physically realistic fashion: they comprise features consistent with a solution of the Navier–Stokes equations.

Efforts to connect wavepackets to, or indeed to derive them from, the Navier–Stokes equations generally involve the use of hydrodynamic stability theory. In view of this we here perform a comparison of the conditional field $\hat{\boldsymbol{q}}$ with the results of linear stability theory for a parallel axisymmetric shear layer (Michalke 1984).

6.1. *Mathematical model*

A linear spatial instability calculation was performed assuming a locally parallel base flow, with inviscid compressible disturbances, as in Michalke (1984). For the base flow, a fit of the linear stochastic estimation mean velocity profile based on a tanh profile is used. Numerical results for the eigenvalue problem were obtained with a Runge–Kutta

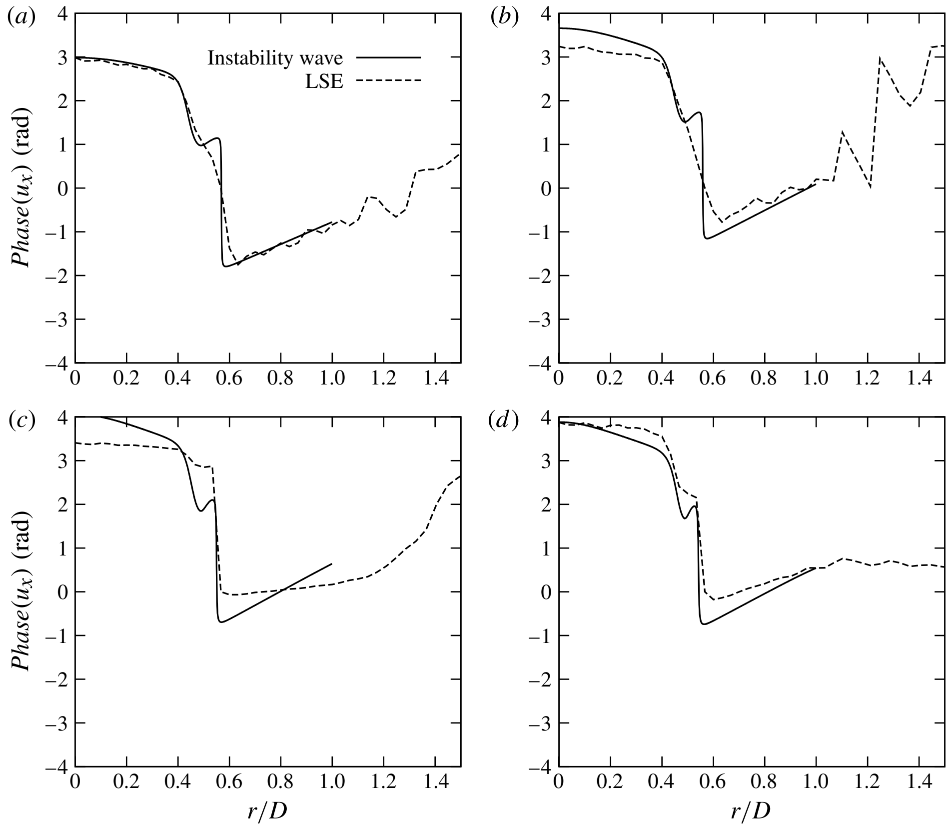

FIGURE 22. Comparison of the phase for the u_x eigenfunctions of linear stability theory and the LSE results at $x/D = 1.5$ for Strouhal numbers of (*a*) 0.40, (*b*) 0.50, (*c*) 0.60 and (*d*) 0.70.

integration in a shooting procedure. As a check of the numerical procedure, the algorithm was seen to reproduce growth rates and convection speeds from Michalke & Hermann (1982). The instability-wave *Ansatz* takes the form

$$\begin{bmatrix} p(x,r) \\ u_x(x,r) \\ u_r(x,r) \\ u_\phi(x,r) \\ \rho(x,r) \end{bmatrix} = C \begin{bmatrix} \tilde{p}(r) \\ \tilde{u}_x(r) \\ \tilde{u}_r(r) \\ \tilde{u}_\phi(r) \\ \tilde{\rho}(r) \end{bmatrix} \exp[\mathrm{i}(\omega t - \alpha x - m\phi)]. \tag{6.1}$$

We consider only the axisymmetric mode, as it is this flow motion – predominant where low-angle sound emission is concerned – that the conditional analysis was constructed to educe from the data. Comparisons are performed at two axial positions, $x/D = 1.5$, the most upstream point, where the wavepackets are in a very early stage of amplification, and $x/D = 3$, where the wavepacket amplitudes peak.

The conditional pressure field is used in both cases to determine the constant C in (6.1); the fluctuation amplitudes of both the axial and radial velocity components of the instability waves are constrained by the pressure matching. The velocity comparisons therefore constitute quite a demanding test of the eduction procedure

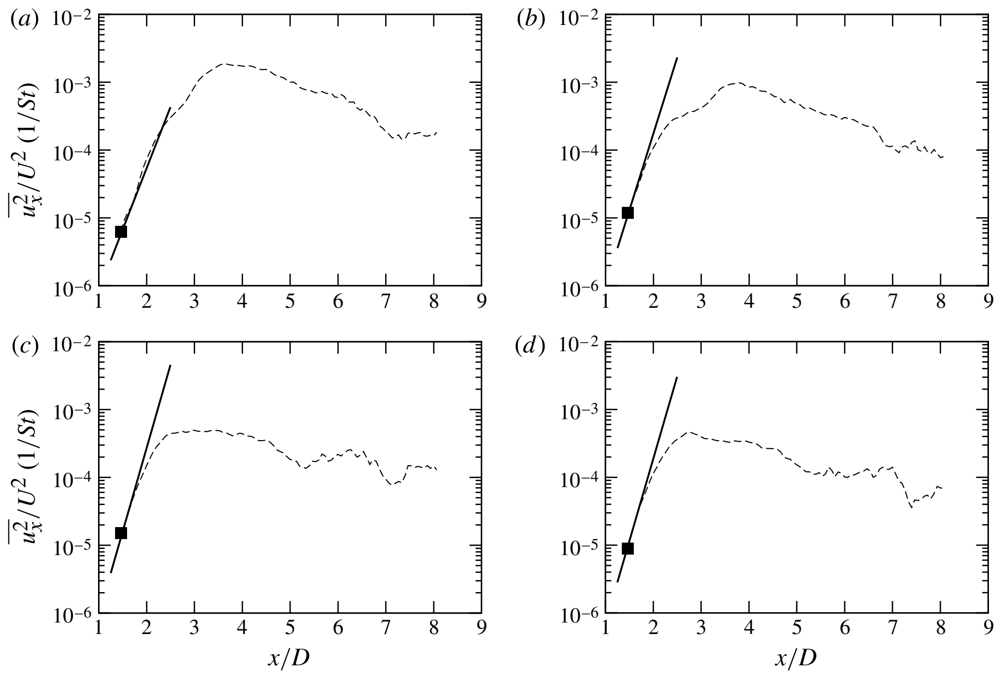

FIGURE 23. Amplitude of the axial velocity fluctuations on the jet centreline from LSE (dashed lines) and growth rate from linear stability at $x/D = 1.5$ (solid lines), for Strouhal numbers of (*a*) 0.40, (*b*) 0.50, (*c*) 0.60 and (*d*) 0.70. Values at $x/D = 1.5$ are highlighted with a square.

(recall that the two velocity components are estimated, independently, both from one another and from the pressure).

The amplification rate is shown in figure 18 as a function of Strouhal number for the two axial locations considered.

6.2. *Linear instability waves in the upstream portion of the jet*

Figure 19 shows a comparison, at $x/D = 1.5$, between the pressure eigenfunctions for four frequencies close to the most unstable frequency of the axisymmetric wave, $m = 0$, and the results of linear stochastic estimation (LSE). The free constant C was adjusted for a best fit with the LSE pressure.

Good agreement is observed between the radial shape of the pressure field obtained by LSE and that of the linear stability eigenfunctions. Both present a maximum near the jet lipline, with exponential decay as r increases. The agreement with axisymmetric linear instability waves suggests, as did the results of § 5, that LSE successfully extracts axisymmetric wavepackets from the full velocity data.

For large r the LSE results show a switch to the algebraic decay characteristic of acoustic waves. The linear instability calculation, on the other hand, based on the parallel flow assumption, does not capture acoustic radiation for subsonically convected waves, which is why the stability eigenfunctions continue to decay exponentially.

Comparison between the linear stability velocity eigenfunctions and the velocity field computed by LSE are shown in figures 20 and 21 for the axial and radial velocity

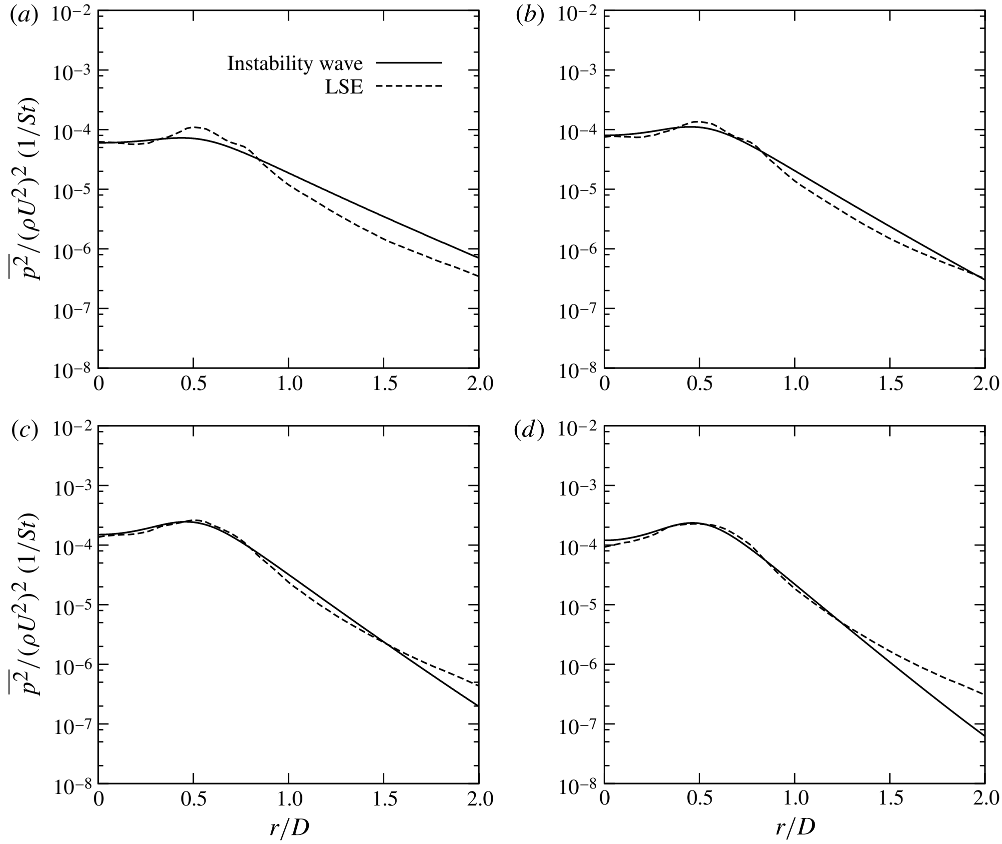

FIGURE 24. Comparison between pressure eigenfunctions of linear stability theory and the pressure field computed by LSE at $x/D = 3$ for Strouhal numbers of (*a*) 0.20, (*b*) 0.25, (*c*) 0.30 and (*d*) 0.35.

components respectively. Recall again that the amplitude of the LST eigenfunctions (the constant C) has been fixed by the pressure matching. Remarkable agreement is observed for both components of the LSE velocity field.

An interesting feature of both the radial shape of the eigenfunctions, shown in figure 20, and which is also observed in the LSE velocity field, is the near-zero amplitude close to the lipline. For the stochastic estimation this is more pronounced for higher Strouhal numbers. As the results of figure 11 show that the estimated field has a topology comprising a convected train of vortical structures, this near-zero amplitude of the axial velocity fluctuation can be understood to be due to the signature of this convected train, which in an idealized case will have zero axial velocity fluctuation at the radial position of the trajectory of the centroid of the vortices. A second feature of such a convected train, as modelled for instance by Lau *et al.* (1972), is a phase inversion. This signature is also observed in both the LST and LSE results, as shown in figure 22.

Finally, figure 23 compares the growth rate computed by LST with the growth rate of the amplitude of the axial velocity fluctuation computed by LSE. The exponential growth rates predicted by LST are shown as straight lines; if these are tangent to the

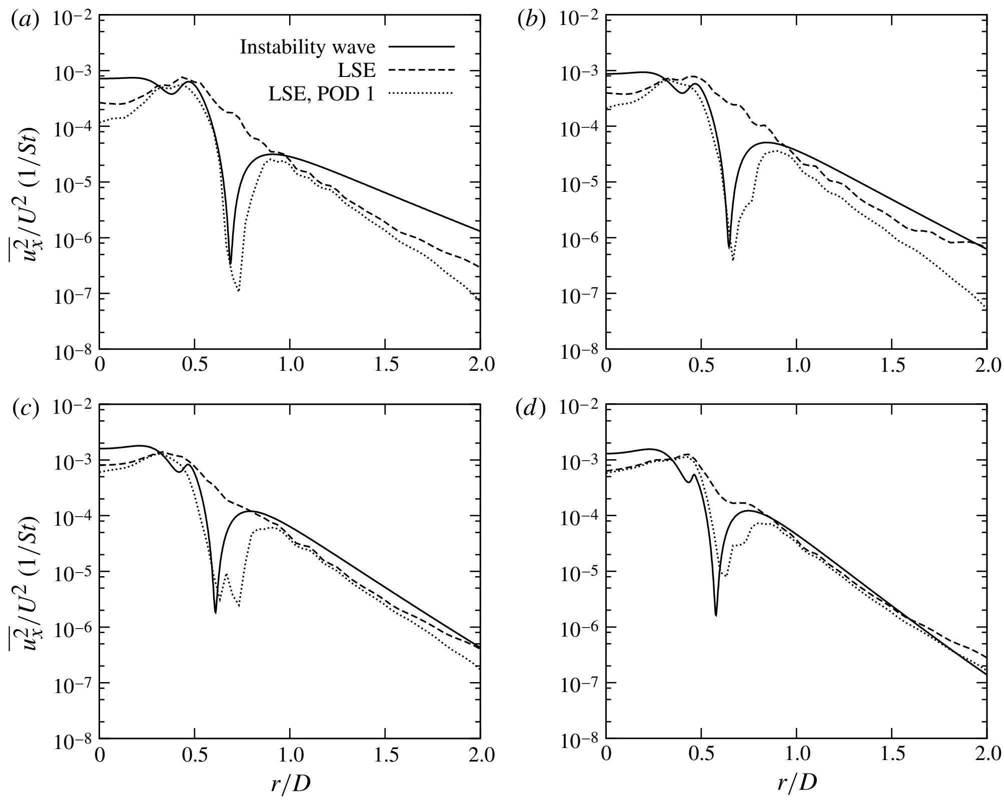

FIGURE 25. Comparison between u_x eigenfunctions of linear stability theory and the corresponding components of the conditional velocity field computed by LSE at $x/D = 3.0$ for Strouhal numbers of (*a*) 0.20, (*b*) 0.25, (*c*) 0.30 and (*d*) 0.35.

curves showing the amplitude of the LSE velocity fluctuations this implies that the local growth rate of the conditional field agrees with the predictions of LST. Similar agreement (not shown) is observed for the growth rates of the pressure and radial velocity fluctuations.

6.3. *Downstream development of instability waves*

The wavepackets educed from the large eddy simulation, shown in § 5 to radiate a quantitatively correct sound field, have their peak amplitude at around $x/D = 3$, after which they decay. This decay is, of course, a crucial part of the sound radiation process. The amplification rates predicted by LST (figure 18) indicate that amplification has considerably weakened at this axial position and that linear instabilities would indeed be on the point of becoming stable. We therefore repeat the same series of comparisons with the predictions of LST at this axial position, in order to ascertain if LST can again be considered a pertinent theoretical context within which to interpret the results of the analysis methodology we have pursued, and to understand the sound-producing decay of the wavepackets.

Comparisons are shown in figures 24, 25, 26 and 27 for four frequencies in the vicinity of the peak of the amplification curve (figure 18). The pressure fit is again used to determine the constant C. Because at this point in the flow the motion of

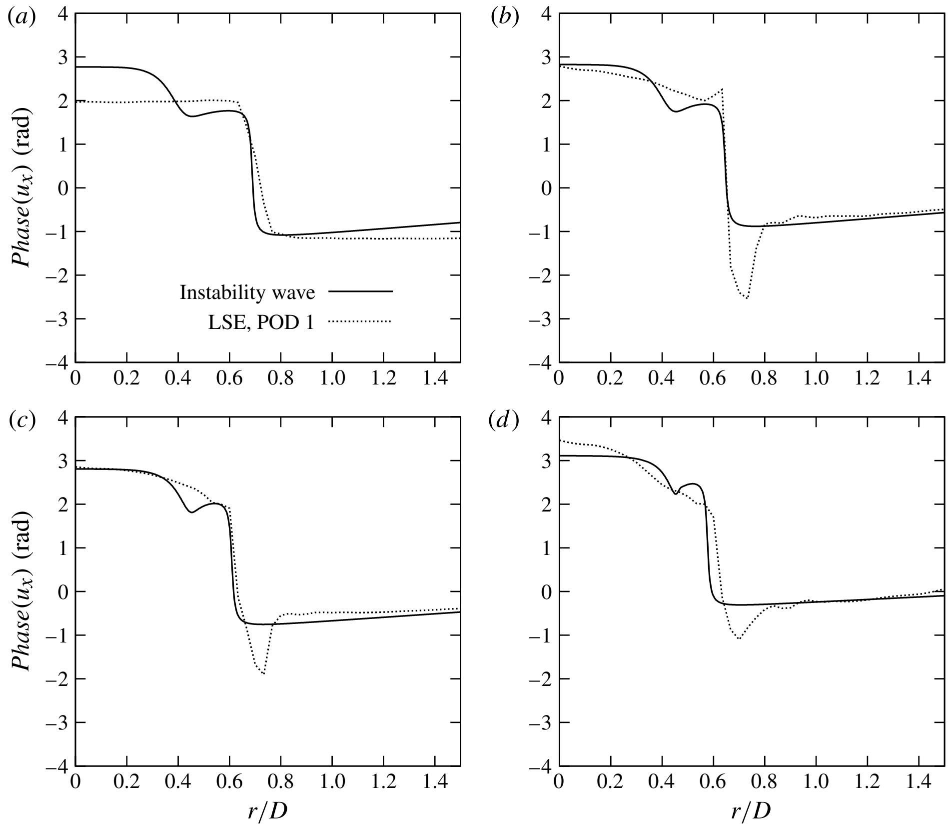

FIGURE 26. Comparison of the phase of the u_x eigenfunctions of linear stability theory and that of the conditional velocity field computed by LSE at $x/D = 3.0$ for Strouhal numbers of (*a*) 0.20, (*b*) 0.25, (*c*) 0.30, (*d*) 0.35.

the vortical structures is more chaotic (they jitter both in x and in r), the near-zero amplitude signature observed at the upstream location does not register so clearly. Application of spectral POD, in the same manner as Gudmundsson & Colonius (2009) and Cavalieri *et al.* (2012*b*), allows this feature of the signature to be extracted. Globally, the agreement is once again remarkably good, indicating that the conditional velocity field educed from the LES is, at its peak amplitude, again synonymous with a linear instability of the mean flow.

7. Conclusions and perspectives

An analysis methodology, developed for the mining of numerical and experimental data in order to understand the flow physics associated with turbulent jet noise, has been presented and applied to a well-documented LES database.

The work is motivated by a desire to go beyond the limits associated with techniques currently used for sound-source identification: acoustic analogies, source imaging (beamforming, etc. ...), two-point flow–acoustic correlations. The core idea consists in using the sound field together with the turbulence field (pressure and velocity) to educe from the turbulent jet to its sound-producing skeleton. Implicit is the idea that underlying the high-dimensional jet turbulence are more organized motions,

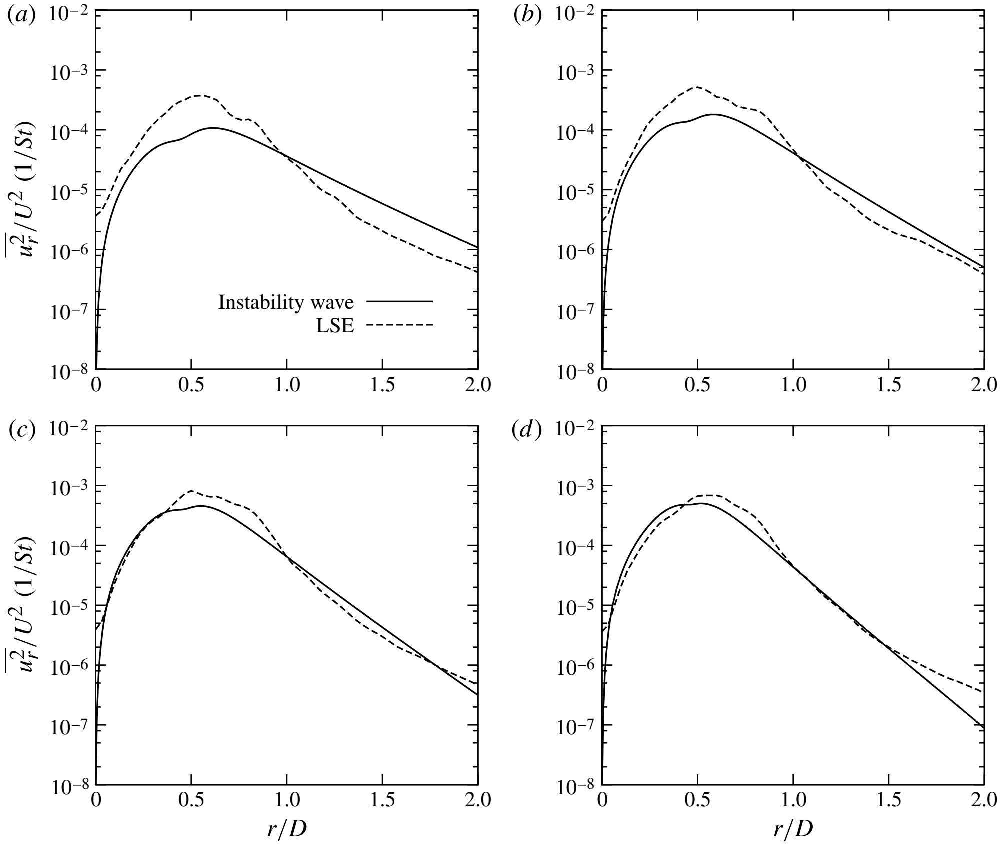

FIGURE 27. Comparison between u_r eigenfunctions of linear stability theory and the corresponding components of the conditional velocity field computed by LSE at $x/D = 3.0$ for Strouhal numbers of (*a*) 0.20, (*b*) 0.25, (*c*) 0.30 and (*d*) 0.35.

often referred to in the literature as coherent structures or wavepackets (Jordan & Colonius 2013).

The educed flow skeleton comprises axially non-compact, space- and time-modulated wavepackets, and is validated in terms of its acoustic behaviour using a line-source *Ansatz*. The acoustic efficiency of the wavepackets is found to be associated with a fixed phase relationship that exists between the spatial and temporal components of the modulation: the time-varying amplitudes and axial length scales are correlated.

The educed structure is, furthermore, tightly correlated with linear instability waves. The meaning of this result can be clarified by considering what lies behind (3.4) outlined by Adrian (1977): linear stochastic estimation provides an approximation of a conditional average. Where jets are concerned, a nice early illustration of a conditional average, and which can be used here to briefly discuss the underlying significance, is provided by the images of Moore (1977) (reproduced here in figure 28). The wavy patterns in figure 28 were obtained by conditionally selecting, and subsequently averaging, Schlieren images corresponding to high-amplitude spikes of the near-field pressure. The fact that the conditional average produces this result, rather than

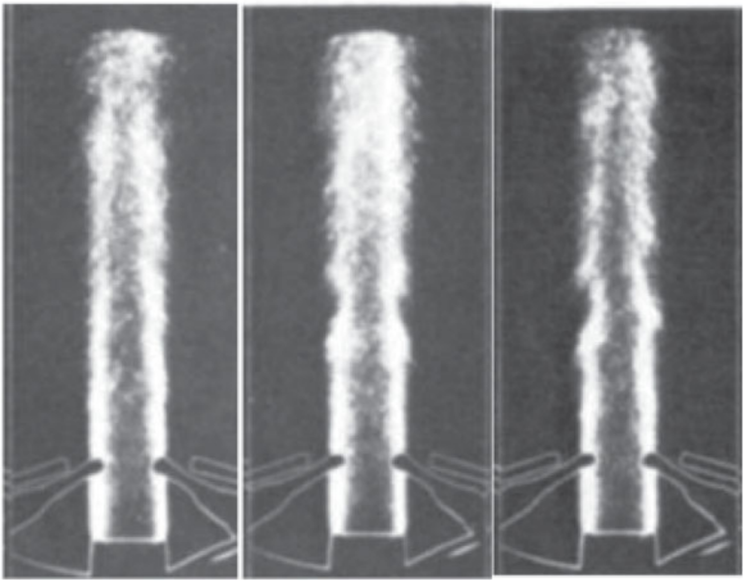

FIGURE 28. Conditional flow visualization from Moore (1977) of a round jet.

something similar to the unconditional average, has a strong implication: it indicates that the wavelike state is real, and is revisited repeatedly by the flow. Keefe (talk cited by Broze & Hussain 1994) has suggested that this indicates the existence of an underlying attractor. It furthermore indicates that the near pressure field contains the signature of these repeated visitations.

It is also well known that the near pressure field of jets is dominated by such wavelike motions (Mollo-Christensen 1963, 1967; Picard & Delville 2000; Tinney & Jordan 2008). Suzuki & Colonius (2006) have placed this observation on a more quantitative footing, showing, in a statistical sense, that the near pressure field of turbulent jets can be associated with linear instabilities of the mean flow; and Reba *et al.* (2010) have shown that it is possible to make the connection between measurements of these instabilities and the far field. Note that the inverse operation, i.e. obtaining the near-field pressure from the far acoustic field, is less straightforward, as it is non-unique; finding the velocity fluctuations from the acoustic far field has never, to the best of our knowledge, been attempted.

With these ideas in mind let us reconsider the main result of the present work, which is that the low-angle component of the acoustic field educes conditional pressure and velocity fields that are strongly identified, in a statistical sense, with axisymmetric linear instability waves: both the growth rates and the (off-axis) radial structures of the waves are obtained. Furthermore, the educed field comprises the saturation and decay phases characteristic of instability waves, and which are so important for sound radiation (Crow & Champagne 1971; Michalke & Fuchs 1975; Ffowcs Williams & Kempton 1978; Tam & Burton 1984*a*,*b*; Crighton & Huerre 1990); but no *a priori* assumption is made that the waves should behave in this way. It is true that the source *Ansatz* used, subsequently, to extract time-varying amplitudes and length scales does contain this growth-to-decay cycle, implicitly, but this behaviour is clearly present in the educed field prior to any consideration of the said *Ansatz*.

These results constitute a further compelling demonstration that the dynamics of the aforesaid attractor can be represented statistically as linear instability waves of the mean flow, and that these are, furthermore, directly related to the low-angle, low-frequency sound radiation. The result therefore provides evidence, complementary to the work of Suzuki & Colonius (2006) and Reba, Simonich & Schlinker (2008) but going beyond it, in the following ways: (*a*) we did not explicitly set out to find instability waves; (*b*) we educe and study both the velocity and the pressure components of the field; (*c*) we use the far-field sound to perform the eduction; and (*d*) we extract space- and time-dependent fields. The work allows us to conclude that the low-angle far-field sound is driven by the dynamics of linear instabilities.

Much of the above reasoning is based on a time-averaged view of things. As per point (*d*), a further novelty of the present work lies in the eduction of space- and time-dependent conditional fields. The particularities of the space–time structure of the educed field (the wavepacket envelope modulations shown to be important where sound generation is concerned; the fact that twenty degrees of freedom suffice to capture the sound radiation; the correlation between the amplitude and length scale), constitute a richer set of clues – than does the favourable comparison with stability theory – regarding the specific morphology of the attractor, and these clues will be important in guiding future modelling efforts.

Acknowledgements

This work was partially supported by the Agence Nationale de la Recherche (ANR-05-BLAN-0208-02) through the programme BruitAero, the French project REBECCA (convention no. 08 2 90 6534) and the EU–Russian programme ORINOCO. A.V.G.C. was supported by CNPq, the National Council of Scientific and Technological Development of Brazil.

REFERENCES

ADRIAN, R. J. 1977 On the role of conditional averages in turbulent theory. In *Turbulence in Liquids: Proceedings of the Fourth Biennial Symposium on Turbulence in Liquids* (ed. G. Patterson & J. Zakin), pp. 322–332. Science Press.

ADRIAN, R. J. 1978 Structural information obtained from analysis using conditional vector events: a potential tool for the study of coherent structures. In *Coherent Structures of Turbulent Boundary Layers,* vol. 22 (ed. C. R. Smith & D. E. Abbot). pp. 2065–2070.

ADRIAN, R. J. 1996 Stochastic estimation of the structure of turbulent fields. In *Courses and Lectures-International Centre for Mechanical Sciences*, pp. 145–196. Springer.

BAILLY, C., BOGEY, C. & MARSDEN, O. 2010 Progress in direct noise computation. *Intl J. Aeroacoust.* **9** (1–2), 123–143.

BODONY, D. J. & LELE, S. K. 2008 Low-frequency sound sources in high-speed turbulent jets. *J. Fluid Mech.* **617** (1), 231–253.

BOGEY, C. & BAILLY, C. 2006*a* Computation of a high Reynolds number jet and its radiated noise using large eddy simulation based on explicit filtering. *Comput. Fluids* **35** (10), 1344–1358.

BOGEY, C. & BAILLY, C. 2006*b* Investigation of downstream and sideline subsonic jet noise using large eddy simulations. *Theor. Comput. Fluid Dyn.* **20** (1), 23–40.

BOGEY, C. & BAILLY, C. 2006*c* Large eddy simulations of round jets using explicit filtering with/without dynamic Smagorinsky model. *Intl J. Heat Fluid Flow* **27**, 603–610.

BOGEY, C. & BAILLY, C. 2006*d* Large eddy simulations of transitional round jets: influence of the Reynolds number on flow development and energy dissipation. *Phys. Fluids* **18**, 1–14.

BOGEY, C. & BAILLY, C. 2007 An analysis of the correlations between the turbulent flow and the sound pressure fields of subsonic jets. *J. Fluid Mech.* **583**, 71–97.

BROZE, G. & HUSSAIN, F. 1994 Nonlinear dynamics of forced transitional jets: periodic and chaotic attractors. *J. Fluid Mech.* **263** (1), 93–132.

CAVALIERI, A. V. G., DAVILLER, G., COMTE, P., JORDAN, P., TADMOR, G. & GERVAIS, Y. 2011*a* Using large eddy simulation to explore sound-source mechanisms in jets. *J. Sound Vib.* **330**, 4098–4113.

CAVALIERI, A. V. G., JORDAN, P., AGARWAL, A. & GERVAIS, Y. 2011*b* Jittering wave-packet models for subsonic jet noise. *J. Sound Vib.* **330**, 4474–4492.

CAVALIERI, A. V. G., JORDAN, P., GERVAIS, Y., WEI, M. & FREUND, J. B. 2010 Intermittent sound generation and its control in a free-shear flow. *Phys. Fluids* **22**.

CAVALIERI, A. V. G., JORDAN, P., COLONIUS, T. & GERVAIS, Y. 2012*a* Axisymmetric superdirectivity in subsonic jets. *J. Fluid Mech.* **704**, 388–420.

CAVALIERI, A. V. G., RODRIGUEZ, D., JORDAN, P., COLONIUS, T. & GERVAIS, Y. 2012*b* Wavepackets in the velocity field of turbulent jets. In *18th AIAA/CEAS Aeroacoustics Conference, Paper* 2011-2743.

CHANDRSUDA, C., MEHTA, R. D., WEIR, A. D. & BRADSHAW, P. 1978 Effect of free-stream turbulence on large structure in turbulent mixing layers. *J. Fluid Mech.* **85** (4), 603–704.

CHRISTENSEN, K. T. & ADRIAN, R. J. 2001 Statistical evidence of hairpin vortex packets in wall turbulence. *J. Fluid Mech.* **431**, 433–443.

CORDIER, L., ABOU EL MAJD, B. & FAVIER, J. 2010 Calibration of POD reduced-order models using Tikhonov regularization. *Intl J. Numer. Meth. Fluids* **63** (2), 269–296.

CRIGHTON, D. G. & GASTER, M. 1976 Stability of slowly diverging jet flow. *J. Fluid Mech.* **77** (2), 387–413.

CRIGHTON, D. G. & HUERRE, P. 1990 Shear-layer pressure fluctuations and superdirective acoustic sources. *J. Fluid Mech.* **220** (1), 355–368.

CROW, S. C. & CHAMPAGNE, F. H. 1971 Orderly structures in jet turbulence. *J. Fluid Mech.* **48** (3), 547–591.

DELVILLE, J., UKEYLEY, L., CORDIER, L., BONNET, J. P. & GLAUSER, M. 1999 Examination of large-scale structures in a turbulent plane mixing layer. Part 1. Proper orthogonal decomposition. *J. Fluid Mech.* **391**, 91–122.

DIMOTAKIS, P. E. & BROWN, G. L. 1976 The mixing layer at high Reynolds number: large-structure dynamics and entrainment. *J. Fluid Mech.* **78** (3), 535–560.

DRUAULT, P., YU, M. & SAGAUT, P. 2010 Quadratic stochastic estimation of far-field acoustic pressure with coherent structure events in a 2D compressible plane mixing layer. *Intl J. Numer. Meth. Fluids* **62** (8), 906–926.

FARGE, M. 1992 Wavelet transforms and their applications to turbulence. *Annu. Rev. Fluid Mech.* **24** (1), 395–458.

FFOWCS WILLIAMS, J. E. & KEMPTON, A. J. 1978 The noise from the large-scale structure of a jet. *J. Fluid Mech.* **84**, 673–694.

FREUND, J. B. 2003 Noise-source turbulence statistics and the noise from a Mach 0.9 jet. *Phys. Fluids* **15**, 1788.

FREUND, J. B. & COLONIUS, T. 2009 Turbulence and source-field POD analysis of a turbulent jet. *Intl J. Aeroacoust.* **8** (4), 337–354.

FUCHS, H. V. & MICHEL, U. 1978 Experimental evidence of turbulent source coherence affecting jet noise. *AIAA J.* **16**, 871–872.

GUDMUNDSSON, K. & COLONIUS, T. 2009 Parabolized stability equation models for turbulent jets and their radiated sound. In *15th AIAA/CEAS Aeroacoustics Conference, Paper* 2009-3380.

GUDMUNDSSON, K. & COLONIUS, T. 2011 Instability wave models for the near-field fluctuations of turbulent jets. *J. Fluid Mech.* **689** (1), 97–128.

GUEZENNEC, Y. G. 1989 Stochastic estimation of coherent structure in turbulent boundary layers. *Phys. Fluids* A **1** (1), 1054–1060.

HUDY, L. M. & NAGUIB, A. 2007 Stochastic estimation of a separated-flow field using wall-pressure-array measurements. *Phy. Fluids* **19**.

HUSSAIN, A. K. M. F. 1983 Coherent structures: reality and myth. *Phys. Fluids* **26** (10), 2816–2850.

HUSSAIN, A. K. M. F. & ZAMAN, K. B. M. Q 1981 The 'preferred mode' of the axisymmetric jet. *J. Fluid Mech.* **110**, 39–71.

JORDAN, P. & COLONIUS, T. 2013 Wavepackets and turbulent jet noise. *Annu. Rev. Fluid Mech.* **45**.

JORDAN, P. & GERVAIS, Y. 2008 Subsonic jet aeroacoustics: associating experiment, modelling and simulation. *Exp. Fluids* **44** (1), 1–21.

JORDAN, P., SCHLEGEL, M., STALNOV, O., NOACK, B. R. & TINNEY, C. E. 2007 Identifying noisy and quiet modes in a jet. In *13th AIAA/CEAS Aeroacoustics Conference, Paper* 2007-3602.

JORDAN, P. & TINNEY, C. E. 2008 The near-field pressure of co-axial subsonic jets. *J. Fluid Mech.* **611**, 175–204.

JORDAN, P., TINNEY, C. E., DELVILLE, J., COIFFET, F., GLAUSER, M. & HALL, A. 2005 Low-dimensional signatures of the sound production mechanism in subsonic jets: towards identification and control. In *35th AIAA Fluid Dynamics Conference, Paper* 2005-4647.

JUVÉ, D., SUNYACH, M. & COMTE-BELLOT, G. 1980 Intermittency of the noise emission in subsonic cold jets. *J. Sound Vib.* **71** (3), 319–332.

KOENIG, M., CAVALIERI, A. V. G., JORDAN, P., DELVILLE, J., GERVAIS, Y. & PAPAMOSCHOU, D. 2011 Farfield filtering of subsonic jet noise: Mach and temperature effects. In *17th AIAA/CEAS Aeroacoustics Conference, Paper* 2011-2926.

LAU, J. C., FISHER, M. J. & FUCHS, H. V. 1972 The intrinsic structure of turbulent jets. *J. Sound Vib.* **22** (4), 379–406.

MANKBADI, R. & LIU, J. T. C. 1984 Sound generated aerodynamically revisited: large-scale structures in a turbulent jet as a source of sound. *Phil. Trans. R. Soc. Lond.* A **311** (1516), 183–217.

MICHALKE, A. 1984 Survey on jet instability theory. *Prog. Aeronaut. Sci.* **21**, 159–199.

MICHALKE, A. & FUCHS, H. V. 1975 On turbulence and noise of an axisymmetric shear flow. *J. Fluid Mech.* **70** (1), 179–205.

MICHALKE, A. & HERMANN, G. 1982 On the inviscid instability of a circular jet with external flow. *J. Fluid Mech.* **114** (1), 343–359.

MOLLO-CHRISTENSEN, E. 1963 Measurements of near-field pressure of subsonic jets. *Tech. rep.* Advisory Group for Aeronautical Research and Development, Paris (France).

MOLLO-CHRISTENSEN, E. 1967 Jet noise and shear flow instability seen from an experimenter's viewpoint. *Trans. ASME: J. Appl. Mech.* **34**, 1.

MOORE, C. J. 1977 The role of shear-layer instability waves in jet exhaust noise. *J. Fluid Mech.* **80** (2), 321–367.

MORRIS, P. J. 2009 A note on noise generation by large-scale turbulent structures in subsonic and supersonic jets. *Intl J. Aeroacoust.* **8** (4), 301–315.

MURRAY, L. & UKEILEY, N. 2005 Velocity and surface pressure measurements in an open cavity. *Exp. Fluids J.* **38** (5), 656–671.

MURRAY, L. & UKEILEY, N. 2007 Modified quadratic stochastic estimation of resonating subsonic cavity flow. *J. Turbul.* **8** (53), 1–23.

OLSEN, M. G. & DUTTON, J. C. 2002 Stochastic estimation of large structures in an incompressible mixing layer. *AIAA J.* **40**, 2431–2438.

PAPAMOSCHOU, D. 2008 Imaging of directional distributed noise sources. In *14th AIAA/CEAS Aeroacoustics Conference and Exhibit, Paper* 2008-2885.

PAPAMOSCHOU, D. 2011 Wavepacket modelling of the jet noise source. In *17th AIAA/CEAS Aeroacoustics Conference, Paper* 2011-2835.

PICARD, C. & DELVILLE, J. 2000 Pressure velocity coupling in a subsonic round jet. *Heat Fluid Flow* **21**, 359–364.

REBA, R., NARAYANAN, S. & COLONIUS, T. 2010 Wave-packet models for large-scale mixing noise. *Intl J. Aeroacoust.* **9** (4), 533–558.

REBA, R., SIMONICH, J. & SCHLINKER, T. 2008 Measurement of source wave-packets in high-speed jets and connection to far-field. In *14th AIAA/CEAS Aeroacoustics Conference, Paper* 2008-2091.

SANDHAM, N. D., MORFEY, C. L. & HU, Z. W. 2006 Sound radiation from exponentially growing and decaying surface waves. *J. Sound Vib.* **294** (1–2), 355–361.

SANDHAM, N. D. & SALGADO, A. M. 2008 Nonlinear interaction model of subsonic jet noise. *Phil. Trans. R. Soc.* A **366** (1876), 2745–2760.

SCHLEGEL, M., NOACK, B. R., JORDAN, P., DILLMANN, A., GROSCHEL, E., SCHRODER, W., WEI, M., FREUND, J. B., LEHMANN, O. & TADMOR, G. 2012 On least-order flow representations for flow aerodynamics and acoustics. *J. Fluid Mech.* **697**, 367–398.

SINAYOKO, S., AGARWAL, A. & HU, Z. 2011 Flow decomposition and aerodynamic sound generation. *J. Fluid Mech.* **668**, 335–350.

SIROVICH, L. 1987 Turbulence and the dynamics of coherent structures. Parts 1–3. *Q. Appl. Math.* **45**, 561–590.

STANISLAS, M., PERRET, L. & FOUCAULT, J. M. 2008 Vortical structures in the turbulent boundary layer: a possible route to universal representation. *J. Fluid Mech.* **602**, 327–382.

SUZUKI, T. & COLONIUS, T. 2006 Instability waves in a subsonic jet detected using a near-field phased microphone array. *J. Fluid Mech.* **565**, 197–226.

TADMOR, G., BISSEX, D., NOACK, B., MORZYNSKI, M., COLONIUS, T. & TAIRA, K. 2008 Temporal-harmonic specific POD mode extraction. In *4th AIAA Flow Control Conference, Paper* 4190.

TAM, C. K. W. & BURTON, D. E. 1984*a* Sound generated by instability waves of supersonic flows. Part 1. Two-dimensional mixing layers. *J. Fluid Mech.* **138**, 249–272.

TAM, C. K. W. & BURTON, D. E. 1984*b* Sound generated by instability waves of supersonic flows. Part 2. Axisymmetric jets. *J. Fluid Mech.* **138** (1), 273–295.

TAM, C. K. W. & MORRIS, P. J. 1980 The radiation of sound by the instability waves of a compressible plane turbulent shear layer. *J. Fluid Mech.* **98** (2), 349–381.

TINNEY, C. E., GLAUSER, M. N. & UKEILEY, L. 2005 The evolution of the most energetic modes in high subsonic Mach number turbulent jets. In *43rd AIAA Aerospace Science, Paper* 2005-0417.

TINNEY, C. E. & JORDAN, P. 2008 The near-field pressure surrounding co-axial subsonic jets. *J. Fluid Mech.* **611**, 175–204.

TINNEY, C. E., JORDAN, P., HALL, A., DELVILLE, J. & GLAUSER, M. N. 2006 A study in the near pressure field of co-axial subsonic jets. In *12th AIAA/CEAS Aeroacoustics Conference, Paper* 2006-2589.

TINNEY, C. E., JORDAN, P., HALL, A. M., DELVILLE, J. & GLAUSER, M. N. 2007 A time-resolved estimate of the turbulence and sound source mechanisms in a subsonic jet flow. *J. Turbul.* **8** (7), 1–20.

TORRENCE, C. & COMPO, G. 1998 A practical guide to wavelet analysis. *Bull. Am. Meteorol. Soc.* **79** (1), 61–78.

TUNG, T. C. & ADRIAN, R. J. 1980 Higher-order estimates of conditional eddies in isotropic turbulence. *Phys. Fluids* **23**, 1469–1470.

UKEILEY, L., CORDIER, L., MANCEAU, R., DELVILLE, J., GLAUSER, M. & BONNET, J. P. 2001 Examination of large-scale structures in a turbulent plane mixing layer. Part 2. Dynamical systems model. *J. Fluid Mech.* **441**.

YULE, A. J. 1978 Large-scale structure in the mixing layer of a round jet. *J. Fluid Mech.* **89**, 413–432.

ZHOU, J., ADRIAN, R. J., BALACHANDAR, S. & KENDALL, T. M. 1999 Mechanisms for generating coherent packets of hairpin vortices in channel flow. *J. Fluid Mech.* **387**, 353–396.